Reviews

Dopants in nanocrystalline tin dioxide

M. N. Rumyantseva, O. V. Safonova, M. N. Boulova, L. I. Ryabova, and A. M. Gas´kov*

Department of Chemistry, M. V. Lomonosov Moscow State University, Leninskie Gory, 119992 Moscow, Russian Federation. Fax: +7 (095) 939 0998. E-mail: roum@inorg.chem.msu.ru

The review surveys studies aimed at constructing new materials for gas sensors based on nanocrystalline tin dioxide. The influence of doping with various impurities (Pt, Pd, Ru, Rh, Cu, Ni, or Fe) on the composition, microstructure, and electrophysical and sensor properties of nanocrystalline SnO_2 was discussed. The conditions for the preparation of powders and thick and thin SnO_2 films by the wet chemical method and aerosol pyrolysis of organometallic compounds are reported. The mechanism of interaction of pure and doped nanocrystalline SnO_2 with a gas phase was analyzed based on the data from Mössbauer, Auger electron, and X-ray photoelectron spectroscopy and the results of *in situ* Raman spectroscopy, XANES, and conductivity measurements.

Key words: nanocrystalline tin dioxide, doping, microstructure, surface state, adsorption, sensor properties.

Introduction

The influence of adsorbed molecules on the electric properties of semiconducting oxides SnO_2, ZnO, WO_3, and In_2O_3 as well as of more complicated systems, such as $Cr_{2-x}Ti_xO_3$ and $FeNbO_4$, has been actively studied in connection with a search for materials for solid-state gas sensors.[1—3] Among these compounds, nanocrystalline tin dioxide is used most extensively. Tin dioxide serves as a unique material for gas sensors due to some of its fundamental chemical and physical properties. First, since this compound is an n-type wide bandgap semiconductor, the conductivity of SnO_2 is very sensitive to the surface state just in the 300—800 K temperature range, in which redox reactions take place on the surface of oxides. Second, the SnO_2 surface exhibits good absorption properties and reactivity due to the presence of free electrons in the conduction band of SnO_2 and the presence of surface and bulk oxygen vacancies and active chemisorbed oxygen. In addition, SnO_2 can be prepared in a stable highly dispersed state with crystallite sizes of 5—20 nm.

An essential drawback of SnO_2-based chemical sensors is their low selectivity, which does not allow one to separate the contribution made by a particular type of molecules in the gas phase to the total electric signal. One of the ways of improving the selectivity of these sensors is to introduce dopants (generally, transition metals or their oxides), which have a strong effect on the electronic and

Published in Russian in *Izvestiya Akademii Nauk. Seriya Khimicheskaya,* No. 6, pp. 1151—1171, June, 2003.

1066-5285/03/5206-1217 $25.00

catalytic properties of the surface, into a highly dispersed oxide matrix. However, the detailed mechanism of this effect remains unknown because the state of the grain surface is violated by high-energy processes in high vacuum used in conventional methods of analysis of the surface. Hence, these methods are poorly informative in the analysis of ultradispersed systems. The *in situ* studies in a gas phase with controlled composition is a complicated problem, which calls for the development of special approaches.

A broad spectrum of metals and their oxides were tested as dopants in SnO_2. These dopants are generally divided into two groups, *viz.*, catalytic (Pt, Pd, Ru, Rh) and electroactive (In, Sb, Cu, Ni, Mn) dopants.[4—6]

Catalytic dopants have attracted the most attention. Using Pt as an example,[7] it was demonstrated that platinum metals are spread over the SnO_2 surface as clusters of size <2 nm. It is assumed that the clusters catalyze specific chemical interactions of SnO_2 with gases according to one of two mechanisms, *viz.*, chemical or electronic. The chemical mechanism involves a two-step process. Initially, gas molecules are adsorbed on the clusters followed by their interaction with the SnO_2 matrix. The rapid transfer of the adsorbed molecules mediated by the platinum metal clusters, which is known as a spillover effect,[8] leads to an increase in the rate of interaction of SnO_2 with the gas phase. The concentration of free charge carriers in SnO_2 correlates with the partial pressure of molecules in the gas phase. The electronic mechanism involves the direct chemical reaction of molecules from the gas phase with clusters resulting in a change in the oxidation state of platinum metals (for example, reduction of PdO to Pd). This process is accompanied by a change in the electron work function of the SnO_2 surface. In this case, the percolation conductivity of SnO_2 depends on the redox properties of the gas phase.

The addition of electroactive dopants also leads to a change in the concentration of free charge carriers in SnO_2. It is assumed that dopant metals are distributed in the bulk of SnO_2 grains and occupy tin positions in the crystal structure, with the resulting increase in the electrical resistance of the material due to compensation of intrinsic V_O^{2+} donor defects with M_{Sn}^- acceptor doping centers.

The influence of dopants on nanocrystalline systems differs substantially from the classical doping effects in semiconductor crystals of Si, Ge, $A^{II}B^{VI}$, $A^{IV}B^{VI}$, and $A^{III}B^{V}$. In nanocrystalline systems, dopants exert an effect on the electric properties not only when they occupy regular positions in crystal structures but also when they are distributed over the surface of nanoparticles. The ratio between the numbers of atom positions on the surface (N_s) and in the bulk of a crystallite (N_b) in nanocrystalline SnO_2 reaches $N_s/N_b = 0.15—0.30$ depending on the crystallite size.[9] Moreover, the distribution of dopants between the grain bulk and surface, which is initially determined by the synthesis conditions, is labile and can be sensitive to the composition of the gas phase. Synchrotron X-ray diffraction and XANES of nanocrystalline SnO_2 revealed the reversible migration of the Cu^{2+} and Fe^{3+} cations between positions in the bulk of grains and on their surface depending on the composition of the gas phase.[10] The oxidation state of dopant metals (particularly, in positions on the grain surface) can also vary with the composition of the gas phase. Some dopants not only have an effect on the electric properties of SnO_2 but also retard the growth of SnO_2 crystallites. Therefore, a detailed analysis of the effect of dopants on the sensor properties of SnO_2 is a multiparameter problem involving investigation of the composition, microstructure, surface state, and electric and sensor properties of doped materials.

The present review surveys the results of studies of the effect of transition metals Cu, Ni, Fe, Pt, Pd, Ru, and Rh on the microstructure, surface composition, and electrophysical properties of nanocrystalline SnO_2. The conditions for the preparation of thick and thin films of nanocrystalline SnO_2 are described. The results of studies of the effect of the gas phase composition on the surface state and electric properties are generalized. Since these systems are labile, main information was obtained by *in situ* techniques under the conditions of the controlled atmosphere and temperature. Some experimental data concerning the influence of Ru and Fe on the properties of SnO_2 are published for the first time.

Characteristics of SnO_2 as sensor material

Tin dioxide has a tetragonal rutile structure (space group D_{4h}^{14})[11] and is characterized by oxygen deficiency. Its composition can be represented as $SnO_{2-\delta}$, where $10^{-5} < \delta < 10^{-3}$ characterizes the deviation from the stoichiometry.[12] The doubly ionized oxygen vacancies V_O^{2+} serve as main intrinsic defects and determine the electric properties of the material, *viz.*, the electron conductivity and concentration of free charge carriers $n = 2[V_O^{2+}]$. The most probable mechanism of the formation of intrinsic atomic defects in SnO_2 involves the Schottky reaction:

$$O_O = O_{surf} + V_O, \quad (1)$$

$$V_O = V_O^{2+} + 2e. \quad (2)$$

Tin dioxide is a wide bandgap semiconductor with the bandgap $E_g = 3.6$ eV (300 K). The energy level of the doubly ionized oxygen vacancies is 130 meV lower than the conduction band edge.[13] The concentration of oxygen vacancies can be decreased by annealing a material in an oxygen atmosphere, but the conductivity type remains unchanged. The relationships between the synthesis con-

ditions, microstructure, and electric and sensor properties of nondoped SnO_2 were considered in the study.[14]

The nature of the sensor signal in semiconductors is associated predominantly with chemisorption involving free electrons in the subsurface layer of the material.[15] The scheme of changes in the band structure of SnO_2 upon adsorption is shown in Fig. 1. The fragment of this scheme (*a*) presents a band diagram in the semiconductor bulk. The chemisorption of oxygen molecules from air occurs with the involvement of electrons of the SnO_2 conduction band and can be described by the equation

$$0.5\,(O_2)_{gas} + 2\,e = (O^{2-})_{surf}. \qquad (3)$$

This interaction gives rise to a volume charge in the subsurface layer, which leads to bending of the conduction band (E_C), valence band (E_V), and donor (E_D) and acceptor levels (E_A) near the surface (see Fig. 1, *b*). The position of the surface state level (E_{SS}) depends on the nature of surface centers. The shift of the conduction band relative to the Fermi level $\Delta(E_C - E_F)$, the Schottky barrier ($e\Delta V_s$), and the change in the electron affinity ($\Delta\chi$) are responsible for a change in the electron work function $\Delta\Phi$ upon chemisorption:

$$\Delta\Phi = e\Delta V_s + \Delta\chi + \Delta(E_C - E_F). \qquad (4)$$

The concentration of surface centers $(O^{2-})_{surf}$ is controlled by the composition of the gas phase, including the oxygen partial pressure in the synthesis. The change in the structure of the SnO_2 surface depending on the oxidation state is shown in Fig. 2. The completely oxidized surface (see Fig. 2, *a*) is characterized by the presence of bridging O atoms, whose concentration decreases in proportion to the O_2 partial pressure (see Fig. 2, *b*). The completely reduced (see Fig. 2, *c*) surface is virtually devoid of the bridging oxygen atoms. In the presence of other molecules in the gas phase, the surface contains various

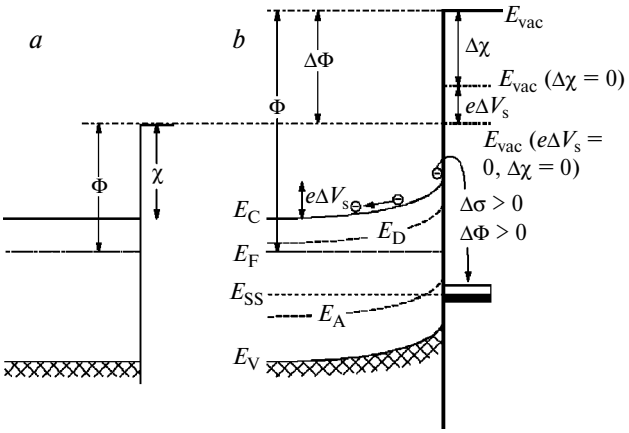

Fig. 1. Electronic band structure of SnO_2 under adsorption conditions.

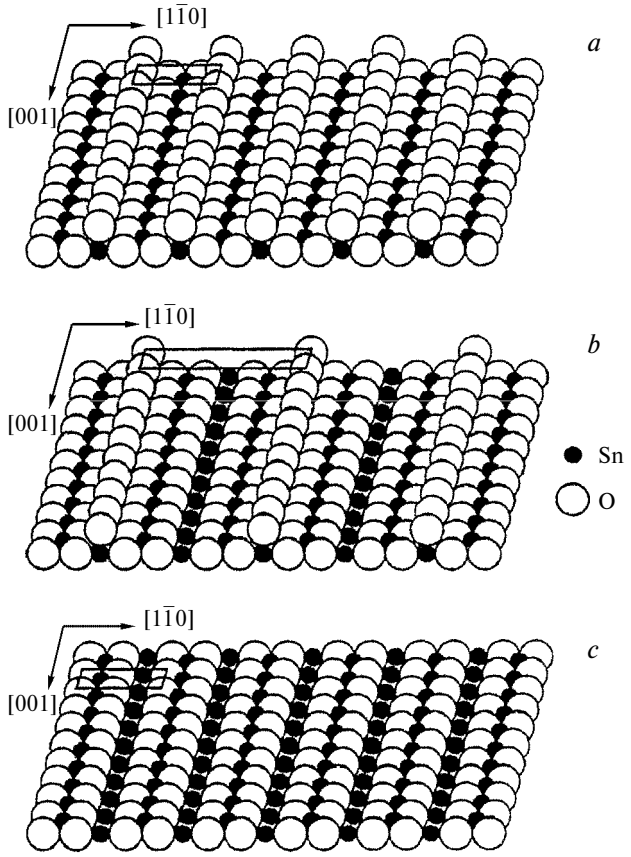

Fig. 2. Structure of the SnO_2 surface: completely oxidized surface (*a*), partially (*b*) and completely reduced surface (*c*).

adsorbed species generated, for example, by the following reactions:

$$CO_{gas} + (O^{2-})_{surf} = (CO_2)_{surf} + 2\,e, \qquad (5)$$

$$(NO_2)_{gas} + e = (NO_2^-)_{surf}, \qquad (6)$$

$$(NO_2^-)_{surf} + e = NO_{gas} + (O^{2-})_{surf}. \qquad (7)$$

The structure and properties of the SnO_2 surface are strongly affected by adsorbed water molecules. The scheme of interactions of H_2O with chemisorbed oxygen molecules is presented in Fig. 3.[16] The resulting surface OH groups can be involved in interactions of SnO_2 with the gas phase.

A change in the conductivity upon adsorption related to $\Delta\Phi$ is determined by the total density of the donor and acceptor centers on the surface. Figure 4 presents the electrical responses of doped SnO_2 films to the periodic changes in the gas atmosphere from dry air to H_2S (Fig. 4, *a*) or NO_2 (Fig. 4, *b*).[17,18] In the presence of H_2S molecules, the conductivity of SnO_2(Cu) increases by a factor of 10^3—10^4, whereas NO_2 molecules have an opposite effect, the maximum effect being observed for SnO_2(Ru). Under these conditions, the conductivity of

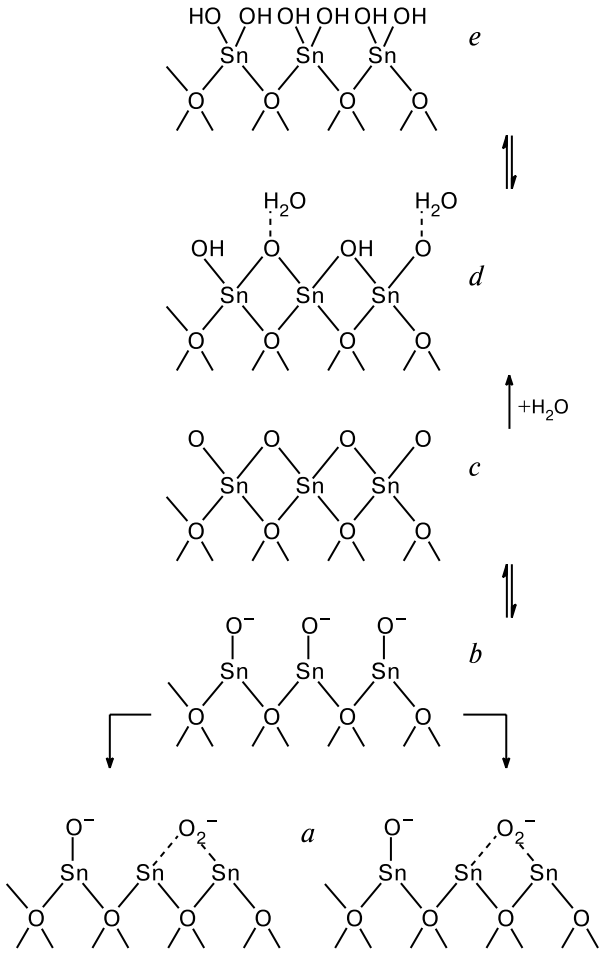

Fig. 3. Scheme of interaction of the SnO_2 surface with H_2O molecules:[16] structure of the SnO_2 surface in the absence (*a*—*c*) and presence of H_2O (*d*, *e*).

nondoped SnO_2 changes insignificantly. The sensor signal S can be calculated from the change in the conductivity (resistance) in air (G_0 (R_0)) and in the presence of the detected gas (G_t (R_t)) as $S = (G_t - G_0)/G_0$ and $S = (R_t - R_0)/R_0$ for reducing and oxidizing gases, respectively. The sensor signals for samples of pure and doped SnO_2 [17—21] are given in Table 1 from which it can be seen that SnO_2(Cu), SnO_2(Ru), and SnO_2(Pd) are of most practical interest for the construction of gas sensors used for the detection of H_2S, NO_2, and CO, respectively.

Synthesis of doped SnO_2

We used the following two methods for the preparation of Pt, Pd, Ru, Rh, Cu, Ni, or Fe-doped SnO_2: aerosol pyrolysis and wet chemical synthesis. The present section reports on the synthesis conditions and characteristics of the resulting compounds, *viz.*, the phase and elemental compositions, microstructure, and surface composition.

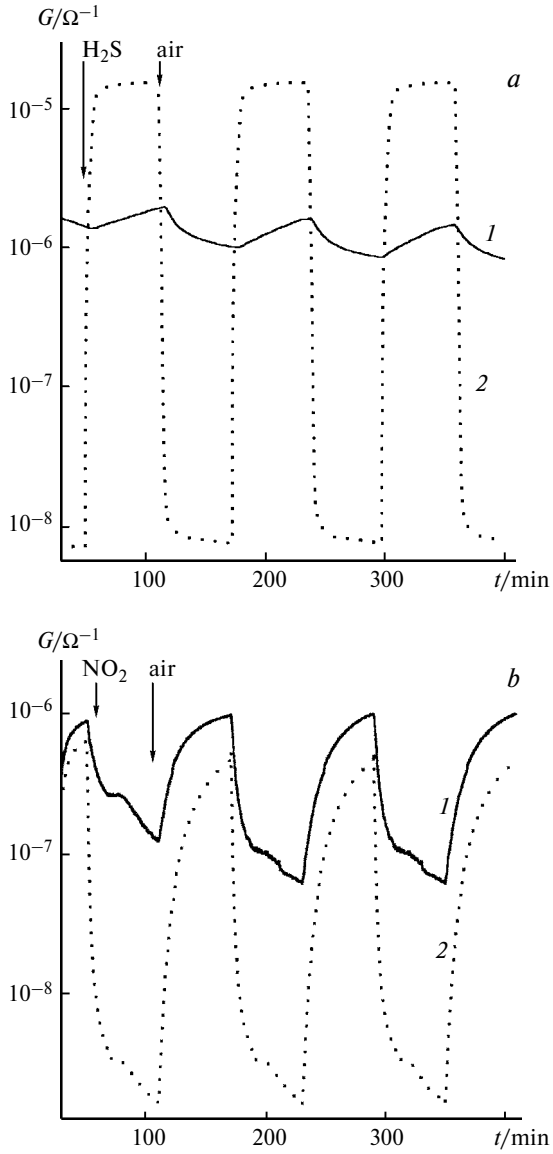

Fig. 4. Changes in the conductivity ($G(t)$) of SnO_2 (*1*) and SnO_2(M) (*2*) in the presence of H_2S (0.01%, 150 °C) (*a*)[18] and NO_2 molecules (50 ppm, 200 °C) (*b*);[17] M = Cu (*a*), Ru (*b*).

The phase composition was determined by powder X-ray analysis on a Siemens Kristalloflex instrument using Cu-Kα radiation. The average size of SnO_2 crystallites (d) was estimated from the broadening of reflections in X-ray patterns according to the Debye—Scherrer equation.[22]

The microstructures of thin films were studied by scanning tunneling microscopy (STM) and transmission electron microscopy (TEM).

Quantitative elemental analysis of thin films was carried out by electron probe microanalysis (EPMA) on a Cameca-SX50 instrument according to a special procedure, which enables one to take into account the influence of the substrate material. Each sample was analyzed

Table 1. Sensor properties of SnO_2-based materials

Material	Type of sample	Gas analyzed	T/°C	Sensor signal S	Reference
SnO_2(Cu)	Thin films	H_2S(0.01%)—N_2	150	10000	19
		EtOH(0.008%)—air	280	10	19
		CO(0.03%)—air	250	3	19
		CH_4(0.1%)—air	300	10	19
		C_3H_8—C_4H_{10}(1%)—N_2	380	2200	20
		H_2(1%)—N_2	380	2500	20
	Thick films	H_2S(0.036%)—N_2	150	36000	20
SnO_2(Ni)	Thin films	H_2S(0.01%)—N_2	260	150	19
		EtOH(0.008%)—air	280	30	21
		CO(0.03%)—air	250	25	21
		CH_4(0.1%)—air	300	10	21
		C_3H_8—C_4H_{10}(1%)—N_2	380	9900	20
		CO(1%)—N_2	380	6400	20
		H_2(1%)—N_2	380	35000	20
SnO_2(Fe)	Thick films	C_3H_8—C_4H_{10}(1%)—N_2	380	950	*
SnO_2(Pd)	Thin films	CO(1%)—N_2	380	5000	20
		H_2(1%)—N_2	380	5700	20
		C_3H_8—C_4H_{10}(1%)—N_2	380	4500	20
		CO(0.03%)—air	100	680	17
		NO_2(0.005%)—air	200	20	17
SnO_2(Pt)	Thin films	CO(1%)—N_2	380	3900	20
		H_2(1%)—N_2	380	1800	20
		C_3H_8—C_4H_{10}(1%)—N_2	380	990	20
SnO_2(Ru)	Thin films	CO(0.03%)—air	250	2	17
		CO(0.03%)—N_2	400	650	17
		NO_2(0.005%)—air	200	290	17
SnO_2(Rh)	Thin films	CO(0.03%)—air	300	1.2	17
		CO(0.03%)—N_2	400	160	17
		NO_2(0.005%)—air	200	30	17

* Our new data.

at six points using four electron beam energies (8, 12, 16, and 20 kV). For each energy, the average characteristic line intensity ratios were calculated for Sn, Si, M, and O in the sample under study and the reference sample ($K_{ratio} = I_i/I_{ref}$). Single crystals of Si and SnO_2 and the corresponding certified metal oxides as ceramics were used as reference samples. The relative errors, which were estimated from the reproducibility of the determination of K_{ratio} after the application of standard ZAF corrections,[23] were at most 5%. The compositions of films were determined by an iteration procedure based on the distribution of X-ray radiation with depth $\varphi(\rho z)$ according to the Pouchou—Pichoir model[23] for a two-layer structure on a single-crystalline silicon substrate with composition $Sn_{1-x}M_xO_2/SiO_2/Si$.

Aerosol pyrolysis is based on thermal decomposition of an aerosol formed upon ultrasound treatment of solutions of organometallic compounds. A 0.2 *M* $Bu_2Sn(AcO)_2$ solution in acetylacetone was used as the starting tin compound. The precursors of dopant metals, the compositions of solutions $[M]_{sol} = 100[M]/([M] + [Sn])$, and the pyrolysis temperatures T_p are given in Table 2.[17,22,24,25] Dry air was used as the carrier gas, whose flow rate was controlled in the course of the synthesis. The aerosol was subjected to thermolysis on the surfaces of heated sub-

Table 2. Conditions of the synthesis of thin SnO_2(M) films by aerosol pyrolysis

M[a]	Precursor	$[M]_{sol}$[b]	T_p[c]/°C	Reference
Cu	$Cu(CF_3COCHCOMe)_2$	0.1—5	460—560	22
Ni	$Ni(Bu(Et)CHCOO)_2$	7—57	460—560	22
Fe	$Fe(acac)_3$	10—40	490—520	[d]
Pd	$Pd(acac)_2$	1.5—7.5	490—520	24
Pt	$Pt(acac)_2$	2.9—10.7	520	25
Ru	$Ru(acac)_3$	1—12	500—540	17
Rh	$Rh(acac)_3$	1—12	500—540	17

[a] Dopant metal.
[b] $[M]_{sol} = 100[M]/([M] + [Sn])$.
[c] Pyrolysis temperature.
[d] Our new data.

strates of oxidized single-crystalline silicon Si <100> or polycrystalline Al_2O_3. The films thus prepared have thicknesses of 0.8—1.0 μm.

According to the results of powder X-ray diffraction analysis, all films thus synthesized contain the only phase, *viz.,* cassiterite SnO_2. No phases containing doping impurities were detected. This may be attributed both to a low content of these phases and small sizes of their crystallites. The reflections of the SnO_2 phase in X-ray diffraction patterns of the films are substantially broadened compared to those in the X-ray diffraction pattern of the microcrystalline sample (Fig. 5). The average crystallite size ($d(SnO_2)$) is in the range of 6—10 nm at different pyrolysis temperatures and depends on the dopant content. In all cases, the introduction of doping impurities led to a decrease in the size of SnO_2 crystallites. This effect, which is shown in Fig. 6 for the films synthesized at 520 °C, can be associated with the partial distribution of the doping impurities over the surface of SnO_2 crystallites as segregations resulting in a decrease in the excess surface energy and elimination of diffusion processes between crystallites.[26]

Electron microscopic studies demonstrated that all the films synthesized have a porous hierarchical structure in which SnO_2 crystallites form agglomerates 50—100 nm in size. The microstructure of the SnO_2(Pd) film investigated by STM is shown in Fig. 7. The crystallite sizes estimated from the microphotographs agree well with their estimates from the broadening of reflections in the X-ray patterns.

The plot of the concentration of dopant metals in the films, $[M]_{film}$, determined by EPMA *vs.* the composition

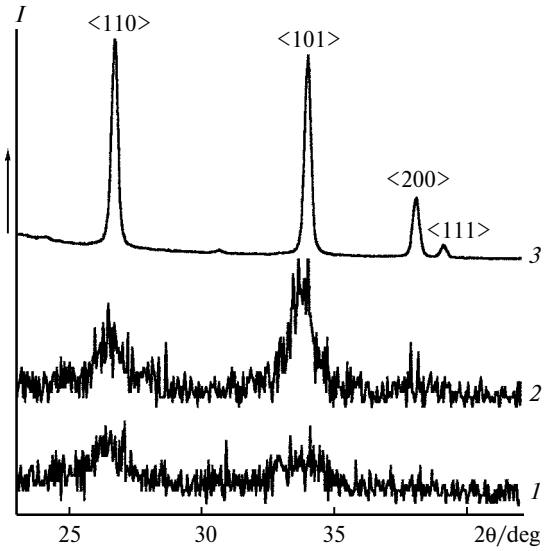

Fig. 5. X-ray diffraction spectra of SnO_2 films with crystallite sizes of 4 (*1*) and 8 nm (*2*);[22] the X-ray diffraction pattern of a microcrystalline SnO_2 powder is presented for comparison (*3*).

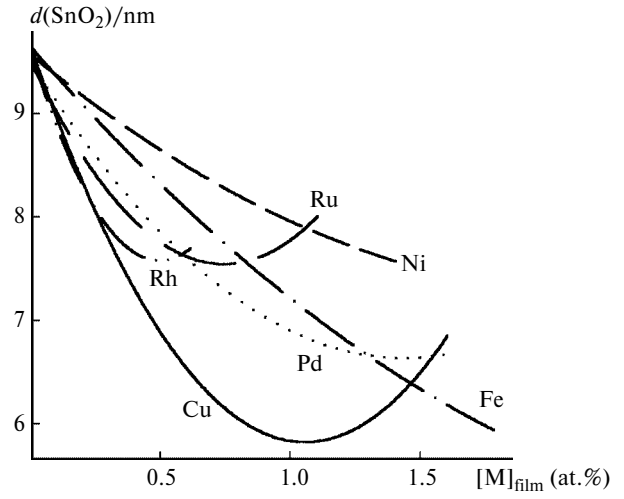

Fig. 6. Average size of SnO_2 crystallites according to X-ray diffraction data ($d(SnO_2)$) depending on the content of doping impurities in films ($[M]_{film}$).[17—22]

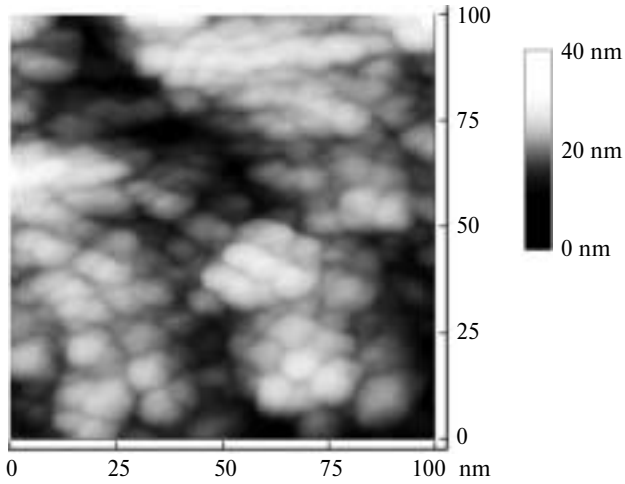

Fig. 7. Image of the SnO_2(Pd) film surface obtained by scanning tunneling microscopy.[17]

of the starting solutions is shown in Fig. 8 for samples synthesized at T_p = 520 °C. The dopant contents in the films were at most 2 at.%. In all cases, the distribution coefficient of dopants between the film and starting solution $K_d = [M]_{film}/[M]_{sol}$ is smaller than unity. The maximum coefficient K_d was observed for copper-doped SnO_2.[22] Aerosol pyrolysis provides a uniform distribution of the doping impurities throughout the thickness of SnO_2 films. The profile of the dopant distribution with thickness of the SnO_2(Pd) film determined by secondary neutral mass-spectrometry (SNMS) is presented in Fig. 9 on the *I*—*t* coordinates, where *I* is the intensity of the mass-spectrum signal proportional to the concentration of the element and *t* is the etching time proportional to the distance from the sample surface.

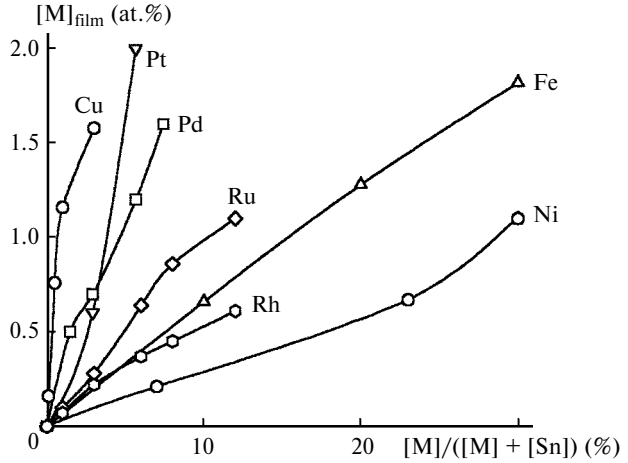

Fig. 8. Plot of the concentration of dopant metals in films ($[M]_{film}$) *vs.* the composition of the starting solution for samples synthesized at T_p = 520 °C.[17—22]

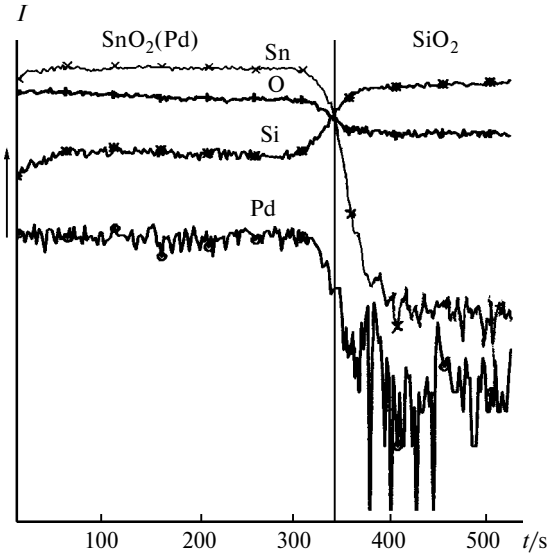

Fig. 9. Depth element distribution of the SnO_2(Pd) film (SNMS);[20] *t* is the etching time proportional to the distance from the sample surface.

Wet chemical method. Powders of SnO_2(M) (M = Cu, Ni, Fe, or Pd) were prepared by thermal decomposition of an α-stannic acid gel followed by impregnation of the product with solutions of the salts of dopant metals.[27,28] The α-stannic acid gel was precipitated by adding an ammonia solution (pH 7.0—7.5) to an aqueous solution of $SnCl_4 \cdot 5H_2O$ with continuous stirring at 0 °C. The precipitate that formed was separated by centrifugation, thoroughly washed-off from chloride ions with distilled water until no reaction with $AgNO_3$ was observed, and dried at 80 °C for one day. Then the powder was impregnated with a solution of the dopant metal salt, dried at 100 °C, and annealed in air at 300, 500, or 700 °C for 24 h. The synthesis conditions and some characteristics of the resulting samples of doped SnO_2 are given in Table 3.

Table 3. Conditions of the synthesis of SnO_2(M) powders by impregnation of a α-stannic acid gel (our new data)

Dopant metal	Precursor	Solution concentration /mol L^{-1}	Content in powder (at.%)	$d(SnO_2)$ /nm (700 °C)
Cu	$Cu(AcO)_2$	0.3	0.5—5.0	24—27
Ni	$Ni(AcO)_2$	0.3	0.5—3.0	13—14
Fe	$Fe(NO_3)_3$	0.5 (+HNO_3)	0.9—8.3	4—22
Pd	$Pd(acac)_2$	0.3 (+AcOH)	1.0	—

Powder X-ray diffraction study demonstrated that all the powders synthesized contained the SnO_2 phase (cassiterite). The CuO and α-Fe_2O_3 phases were found in samples containing >5 at.% of dopant metals. The average size of SnO_2 crystallites varies within 3—30 nm depending on the annealing temperature and powder composition. An increase in the annealing temperature leads to an increase in the size of SnO_2 crystallites (Fig. 10). The introduction of dopants decreases the growth rate of SnO_2 crystallites under the conditions of high-temperature annealing, the maximum effect being observed in the case of nickel and iron (Fig. 11).

Influence of the gas phase on the surface state of SnO_2(M)

Let us consider the results of studies of the influence of the gas phase on the surface state of doped nanocrystalline SnO_2 (surface composition, concentration of

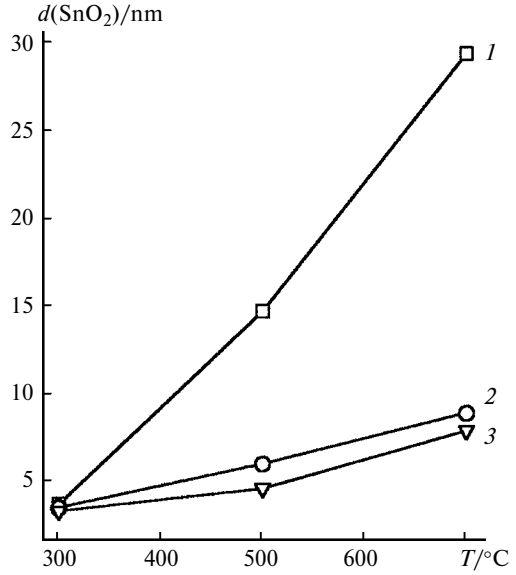

Fig. 10. Changes in the size of SnO_2 crystallites depending on the annealing temperature for SnO_2 (*1*) and SnO_2(Fe) powders containing 2.5 (*2*) and 4.2 at.% of Fe (*3*) (our new data).

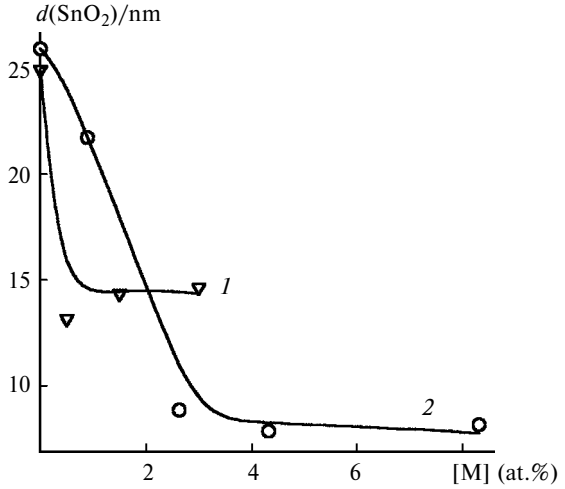

Fig. 11. Changes in the size of SnO_2 crystallites depending on the concentrations of Ni (*1*) and Fe (*2*) in SnO_2(M) powders after annealing at 700 °C (our new data).

chemisorbed oxygen, and deviation of the composition from the stoichiometry) and the electronic states of their own components and dopants. All experiments were carried out with the use of dry synthetic air and certified gas mixtures.

The compositions of the film surfaces were studied by Auger electron spectroscopy (AES) on a Jump 10-CCS (JEOL) instrument.[22] Electron probe microanalysis was carried out using six to eight points in vacuum of $1 \cdot 10^{-9}$ Torr at the incident electron beam energy of 3 kV and passing a current of 10^{-8}—10^{-9} A through samples (diameter of the region analyzed was 0.1 μm and the distance between the points was 5—10 μm). The spectra were recorded in the region from 50 to 550 eV in the differential form $dN(E)/dE$. The film compositions at the depth of 10—30 nm (in the bulk) were studied using ion etching with an Ar^+ beam with the energy of 500 eV (partial Ar pressure was $(5—8) \cdot 10^{-5}$ Torr and the ion current was $1 \cdot 10^{-6}$ A). The results of analysis are represented as the normalized intensity ratio I_O/I_{Sn}. The ratio between the oxygen and tin concentrations C_O/C_{Sn} was calculated using a fresh chip of a SnO_2 single crystal as the reference sample.

The surface state of the films was analyzed by XPS on PHI-5400, Perkin—Elmer, and VG MKII instruments using Mg-Kα or Al-Kα radiation.[20] Pure metallic silver (99.99%) and gold evaporated onto the surface of SnO_2 films as thin layers (~6 nm) were used as reference samples. The spectra were calibrated against the energies of the $Ag3d_{5/2}$ and $Au4f_{7/2}$ electronic levels (368.2 and 83.8 eV, respectively). The $Sn3d_{5/2}$ peak in the spectrum of SnO_2 was used as the internal standard. The electron energies of Sn ($3d_{5/2}$ and $3d_{3/2}$), O1s, C1s, Cu ($2p_{3/2}$), Ni ($2p_{3/2}$), Ru ($3d_{5/2}$ and $3d_{3/2}$), Rh ($3d_{5/2}$ and $3d_{3/2}$), and Pd ($3d_{5/2}$ and $3d_{3/2}$) were determined. The film compositions in the bulk (at the depth of 10—30 nm) were analyzed using ion etching with an Ar^+ beam. The results of analysis are represented as the ratio between the oxygen and tin concentrations (C_O/C_{Sn}), which were calculated with the use of single-crystalline SnO_2 as the reference sample.

The effect of the composition of the gas phase on the chemical state of tin, oxygen, and doping elements present on the surface and in the bulk of SnO_2 and SnO_2(M) films was studied by AES and XPS. The films were annealed in a special quartz cell at 380 °C for 2—4 h using the gas phase with fixed composition. To decrease the time of exposure to air, the films were cooled in the same gas mixture, which was then used for annealing, and immediately placed in an analytical chamber of the spectrometer. The time of exposure of the samples to air was at most 1 min.

Studies of the surface state of SnO_2 films by AES and XPS demonstrated that the films contained no noncontrolled impurities. Carbon on the surface was detected only in the SnO_2(Ru) films. However, its concentration was at most 1—2 at.%. The electronic states of oxygen, tin, and doping elements were analyzed by XPS. The energies of peaks and the reference energies of the corresponding electronic levels are given in Table 4.[19,20]

For all films, the positions of the $Sn3d_{5/2}$ and $Sn3d_{3/2}$ peak maxima correspond to SnO_2.[29] However, the presence of Sn^{2+} in the films must not be ruled out because the energy of $Sn3d_{5/2}$ for SnO (486.5 eV) is very close to that for SnO_2 (486.65 eV). Tin metal in which the energy of $Sn3d_{5/2}$ is 484.9 eV was not found in the films.

The energies of the O1s peak maxima for all films are close to the energy, which is characteristic of the lattice oxygen in the SnO_2 crystal structure (530.6 eV).[29,30] A detailed analysis of the spectrum demonstrated that the peak on the surface is substantially broadened. In addition, the component with the energy of 531.0—533.0 eV also makes a substantial contribution (Fig. 12).[20] This can be attributed to the presence of different forms of

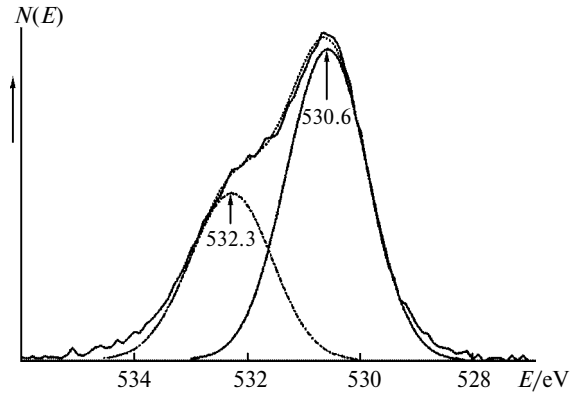

Fig. 12. Data from X-ray photoelectron spectroscopy for O1s in a SnO_2(Pd) film ([Pd] = 1.6 at.%).[20]

Table 4. Positions of peak maxima according to the XPS data for SnO_2 and SnO_2(M) films[19,20] (reference data[29] are given in italic type in parenthesis)

Sample	[M] (at.%)	Region analyzed	$E(Sn3d_{5/2})$	$E(Sn3d_{3/2})$	$E(O1s)$	$E(M2p_{3/2})$	$E(M3d_{5/2})$	$E(M3d_{3/2})$
			eV					
SnO_2	—		(*486.65*)	(*495.15*)	(*530.6*)	—	—	—
SnO_2	—	Surface	486.9	495.3	530.8	—	—	—
		30 nm depth	486.7	495.2	530.6	—	—	—
SnO_2(Cu)	1.26	30 nm depth	487.0	495.2	530.9	933.0 (*933.7*), CuO (*932.6*), Cu_2O	—	—
SnO_2(Ni)	1.25	30 nm depth	487.0	493.2	531.8	833.5 (*833.5*), NiO	—	—
SnO_2(Ru)	1.4	Surface	486.4	495.0	531.3	—	281—282 (*282.1*), RuO_2	—
		30 nm depth	486.4	495.0	530.9	—	282.0 (*282.1*), RuO_2	286.2
SnO_2(Rh)	0.76	Surface	486.4	495.0	530.6	—	—	—
		30 nm depth	486.4	495.0	530.6	—	—	—
SnO_2(Pd)	1.6	Surface	486.9	495.3	530.8	—	337.0 (*336.3*), PdO	342.3
		30 nm depth	486.6	495.1	530.6 (*530.60*)	—	335.4 (*335.2*), Pd; 337.0 (*336.3*), PdO	340.9 342.3

adsorbed oxygen (O_{ads}) on the film surface, *viz.*, O^- (531.2—531.5 eV),[31] O_2^{2-} (532.7 eV),[31] and O_2 (532.6 eV),[32] as well as to the presence of the surface OH^- groups (532.0,[33] 531.8 eV[31]). Etching of samples with Ar^+ ions and high-temperature annealing substantially decrease the contribution from these species.

The ratios between the peak areas of the adsorbed species (O_{ads}, 532.3 eV) and lattice oxygen (O_{SnO_2}, 530.6 eV), determined for the SnO_2(Pd) films after annealing at 380 °C in different gases are given in Table 5.[20] Unexpectedly, the peak area of O_{ads} increased after annealing in an H_2(1%)—N_2 atmosphere. Apparently, this effect is associated with the tendency of the system to regain the initial equilibrium state distorted upon prolonged annealing in a reducing atmosphere. Short-term exposure to air (<1 min) appeared to be sufficient for saturation of the adsorption layer with oxygen. Annealing in an H_2 atmosphere resulted in the maximum contribution of a component with the energy of 532.3 eV, which is indicative of the formation of OH^- groups on the surface. Annealing of the films in a CO atmosphere also led to broadening of the O1s peak, but no high-energy shift of the maximum was observed.

Table 5. Ratio between the peak areas (R_S) (XPS) of adsorbed species (O_{ads}, 532.3 eV) and lattice oxygen (O_{SnO_2}, 530.6 eV)[20]

Atmosphere	R_S	
	Surface	30 nm depth
O_2	0.25	0.16
N_2	0.27	0.14
H_2(1%)—N_2	0.53	0.22

According to the data presented in Table 4, the doping elements in SnO_2 occur in the oxidized state. The position of the $Ru3d_{5/2}$ maximum corresponds to Ru^{4+}. Palladium occurs both in the oxidized (Pd^{2+}) and metallic (Pd^0) states. The oxidation states of ruthenium and palladium correspond to the thermodynamically most stable oxides (RuO_2 and PdO, respectively). The presence of Pd^0 can be attributed to a low heat of formation of PdO and, consequently, to an ease of its decomposition. The oxidation state of rhodium could not be reliably determined because of its low concentration in the films and the problems associated with an induced charge. The electronic state of nickel corresponds to NiO. The data for copper are indicative of the simultaneous presence of two oxides, *viz.*, CuO and Cu_2O. The Cu^+ oxidation state was also observed in studies of the films by AES. This fact can be attributed to the effect of both high vacuum and ion etching on the surface.[34]

Estimation of the dopant effect on the energy of the Sn—O bond is of interest. Analysis of the difference between the energies of the $Sn3d_{5/2}$ (E_1) and O1s (E_2) electronic levels characterizing the Sn—O bond energy provided evidence that the introduction of nickel or ruthenium at concentrations of 1.1—1.2 at.% has a noticeable effect on $\Delta E = E_2 - E_1$. By contrast, palladium and cop-

Table 6. Difference between the energies ($\Delta E = E_2 - E_1$) of the $Sn3d_{5/2}$ and O1s electrons in films of pure and doped SnO_2 and the effective ionic radii (r) of Sn^{4+} and dopant metals

Sample	[M] (at.%)	ΔE/eV	M	r/Å [35]
SnO_2	—	43.95 [29]	—	—
SnO_2	—	44.00±0.05 [19]	Sn^{4+}	0.69
SnO_2(Pd)	1.6	44.00±0.05 [17]	Pd^{2+}	0.86
SnO_2(Cu)	1.2	43.90±0.05 [19]	Cu^{2+}	0.73
SnO_2(Ni)	1.2	44.80±0.05 [19]	Ni^{2+}	0.70
SnO_2(Ru)	1.1	44.70±0.05 *	Ru^{4+}	0.62

* Our new data.

per exert no effect on ΔE (Table 6).[19,20,29] The influence of dopants on ΔE can be associated with the defect formation in the SnO_2 crystal structure due to the replacement of tin by dopants (M_{Sn}). It is assumed that the Ni^{2+} and Ru^{4+} ions can be incorporated into the Sn^{4+} positions on the SnO_2 surface thus changing the Sn—O bond energy. By contrast, copper and palladium are primarily distributed as CuO_x and PdO_x segregations on the SnO_2 grain surface and have only a slight effect on the Sn—O bond energy. This assumption agrees with the effective ionic radii of the elements[35] (see Table 6).

Figure 13 presents the XPS data for Pd3d obtained for the SnO_2(Pd) films after annealing at 380 °C in oxygen (curve *1*), an H_2(1%)—N_2 gas mixture (curve *2*), and nitrogen (curve *3*).[20] The oxidation state of palladium in the films annealed under O_2 corresponds to PdO (342.3 and 337.0 eV). The spectrum recorded for a reduced surface (annealed in an H_2(1%)—N_2 mixture) corresponds to Pd metal (340.8 and 335.6 eV). Palladium was also reduced by annealing in a CO(1%)—N_2 mixture. Annealing in an inert atmosphere of N_2 led to partial reduction of palladium as evidenced by the presence of maxima

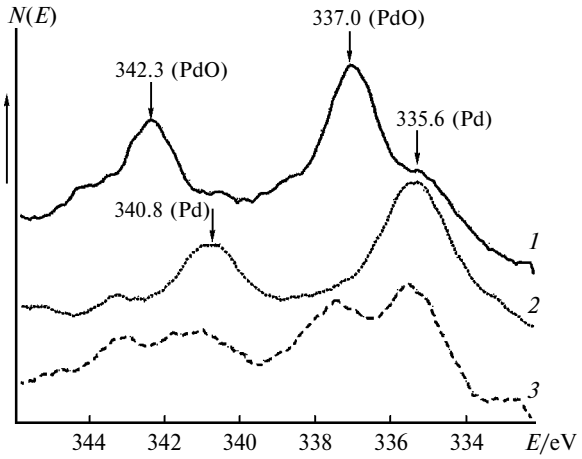

Fig. 13. Data from X-ray photoelectron spectroscopy for Pd3d in a SnO_2(Pd) film ([Pd] = 1.6 at.%) after annealing at 380 °C in oxygen (*1*), an H_2(1%)—N_2 gas mixture (*2*), and nitrogen (*3*).[20]

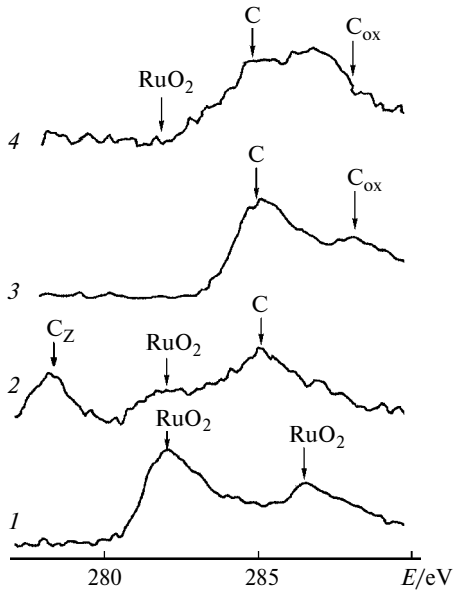

Fig. 14. Data from X-ray photoelectron spectroscopy for Ru3d and C1s on the SnO_2(Ru) film surface ([Ru] = 1.4 at.%) after successive exposure to dry air at 550 °C (*1*), a CO(1%)—N_2 gas mixture at 300 (*2*) and 500 °C (*3*), and dry air at 550 °C (*4*) (our new data); C_Z corresponds to the differential charging of carbon on the film surface.

corresponding to Pd metal and PdO in the spectrum of the product.[20]

Reductive annealing of the SnO_2(Ru) film in a CO(1%)—N_2 gas mixture does not change the oxidation state of ruthenium occurring as Ru^{4+} (Fig. 14). In addition, the reaction of the SnO_2(Ru) film with CO is accompanied by the appearance of carbon-containing impurities on the surface. At 300 °C, the surface is covered with unoxidized carbon (285.0 eV), which leads to substantial problems associated with an induced charge (see Fig. 14, curve *2*). Annealing in a CO atmosphere at higher temperature (500 °C) affords oxidized forms of surface carbon with energies of 285.3—288.0 eV (see Fig. 14, curve *3*). Subsequent annealing in air at 300—550 °C does not completely remove carbon-containing impurities (see Fig. 14, curve *4*). This is a frequently occurring phenomenon in catalysis, which can be attributed to CO disproportionation on the surface:[8]

$$2\,CO \rightarrow C_s + CO_2. \qquad (8)$$

The composition of SnO_2 deviates from the stoichiometry by at most 10^{-2} at.%, which is substantially smaller than the sensitivity of the AES and XPS methods. However, extensive studies of metal oxide surfaces provided evidence that the nonstoichiometry of the subsurface layer may be much higher. The C_O/C_{Sn} ratios for the films of pure and doped SnO_2 calculated from the AES and XPS data are given in Table 7. It can be seen that the film surfaces are enriched in oxygen. This is associated with

Table 7. Ratios between the oxygen and tin concentrations (C_O/C_{Sn}) in films of pure and doped SnO_2 calculated from AES and XPS data[20,36]

Sample	[M] (at.%)	Region analyzed	C_O/C_{Sn}		
			I[a], AES	II[b]	
				AES	XPS
SnO_2	—	Surface	2.4	2.8	2.8
		30 nm depth	1.7	2.2	2.1
SnO_2(Cu)	1.6	Surface	2.4	—	—
		30 nm depth	2.1	—	—
SnO_2(Pt)	0.6	Surface	2.6	2.9	—
		30 nm depth	1.9	—	—
	2.0	Surface	2.5	3.1	—
		30 nm depth	1.9	—	—
	6.3	Surface	2.9	3.4	—
		30 nm depth	2.2	—	—
SnO_2(Ru)	1.4	Surface	—	—	4.0
		30 nm depth	—	—	1.9
SnO_2(Rh)	0.76	Surface	—	—	3.0
		30 nm depth	—	—	1.9
SnO_2(Pd)	1.6	Surface	2.5	3.0	2.8
		30 nm depth	1.8	2.1	2.1

[a] Samples without annealing.
[b] After annealing in air at 380 °C.

adsorption of O_2 molecules and HO^- groups on the SnO_2 surface as well as with the presence of doping oxides. The highest oxygen concentration was found on the SnO_2(Ru) film surface.

Annealing of SnO_2(Pd) in a reducing CO or H_2 atmosphere leads to a decrease in the C_O/C_{Sn} ratio in the bulk but does not decrease the concentration of oxygen on the surface (Table 8).[20,37] In this case, the surface composition depends on the procedure for the preparation of the sample. It was assumed[38] that an excess concentration of the adsorbed oxygen on the surface after annealing in a reducing medium is a consequence of short-term exposure of samples to atmospheric oxygen during their transfer to a spectrometer. The adsorbed oxygen serves as a source compensating the oxygen deficiency in the bulk.

The oxygen content in the SnO_2(Pt) films in relation to the Pt concentration and the conditions of thermal annealing was examined by AES (see Tables 7 and 8).[36] The C_O/C_{Sn} ratios were determined on the surface and after sputtering of a 30-nm layer. In all cases, the C_O/C_{Sn} ratio on the surface is higher than that in the bulk of the film and increases as the Pt concentration increases. Annealing in air leads to an increase in the C_O/C_{Sn} ratio. Annealing of platinum-doped samples in a reducing atmosphere leads to a decrease in the oxygen concentration both in the bulk and on the surface. The plot of C_O/C_{Sn} *vs.* the Pt concentration after annealing in a reducing atmosphere passes through a minimum corresponding to 0.6 at.% of Pt. It is this platinum concentration that corresponds to the maximum gas sensitivity of SnO_2(Pt) toward CO.[36]

Therefore, the investigation of the surface composition of samples after annealing in a reducing atmosphere revealed the difference in the effect of Pt and Pd on the C_O/C_{Sn} ratio. In the case of Pt, the amount of adsorbed oxygen decreases. By contrast, the amount of adsorbed oxygen increases in the presence of Pd. This difference was attributed to the distinction in the rate of the reaction of dopants with atmospheric oxygen. A layer of the excess adsorbed oxygen, which is formed on the SnO_2(Pd) surface upon short-term exposure to air, has no time to be formed on the SnO_2(Pt) surface. The difference in the effect of Pt and Pd on the composition of the SnO_2 surface corresponds to the difference in the standard energies of formation ($\Delta_f H^\circ_{298}$) of stable platinum metal oxides given below.

Oxide	PtO_2	PdO	IrO_2	Rh_2O_3	RuO_2
$-\Delta_f H^\circ_{298}$ /kJ (mol of [O])$^{-1}$	67 [37]	115 [39], 117.4 [40]	127 [39], 124.5 [41]	120 [39], 135.2 [42]	152 [39], 156.8 [43]

Table 8. Ratios between the oxygen and tin concentrations (C_O/C_{Sn}) in films of pure and doped SnO_2 calculated from AES and XPS data[20,37]

Sample	[M] (at.%)	Region analyzed	C_O/C_{Sn}				
			Air, AES	CO(1%)—N_2		H_2(1%)—N_2	
				AES	XPS	AES	XPS
SnO_2	—	Surface	2.8	2.5	—	2.8	—
		30 nm depth	2.2	—	—	1.8	—
SnO_2(Pt)	0.6	Surface	2.9	1.9	—	—	—
	2.0	Surface	3.1	2.4	—	—	—
	6.3	Surface	3.4	2.8	—	—	—
SnO_2(Ru)	1.4	Surface	4.0	—	3.0	—	—
		30 nm depth	1.9	—	—	—	—
SnO_2(Pd)	1.6	Surface	3.0	2.9	2.9	2.9	3.0
		30 nm depth	2.1	2.0	1.9	1.8	1.9

The formation of PdO is more favorable than that of PtO_2. At the same time, ruthenium has the maximum oxygen affinity and one would expect an increase in the oxygen concentration on the surface of SnO_2(Ru) films. However, an opposite effect was experimentally observed, *viz.*, annealing in a reducing CO(1%)—N_2 atmosphere led to a decrease in the oxygen concentration on the ruthenium-doped film surfaces. This can be associated with partial filling of the SnO_2(Ru) surface with carbon-containing impurities, whose removal requires additional annealing in air.

Study of *in situ* SnO_2(M) interaction with the gas phase

XANES study of the electronic state of Pt on the SnO_2 surface. Investigation of the effect of adsorbed molecules on the electronic state of dopants directly in the course of solid state—gas interactions (*in situ*) is of particular importance. As mentioned above, classical procedures for analysis of the surface violate the surface state because of interaction of the surface with the high-energy electron or ion beams in high vacuum. At low concentrations of the dopant, XANES is, in our opinion, the most informative method. Studies by this method were carried out with the use of synchrotron radiation (BM32 line, European Synchrotron Radiation Facility (ESRF), Grenoble, France)[36] employing a two-crystal Si <111> monochromator with a resolution $\Delta E/E = 2 \cdot 10^{-4}$ (beam 0.3 mm × 0.3 mm, photon flux through a sample $2 \cdot 10^{12}$ photon s^{-1}). The emission intensity of the Pt L_{III} white line (11564 eV) was analyzed. The spectra were recorded in the fluorescence mode in the range of 11400—12400 eV. Platinum metal and PtO_2 were used as the reference samples. The spectra of the reference samples were recorded in the transmission mode.

The XANES spectra of SnO_2(Pt) films recorded in air at 350 °C[36] are shown in Fig. 15. Under these conditions, the probability of the Pt $2p_{3/2} \rightarrow 5d$ electron transition depends on the Pt concentration in the films. A comparison of these results with the spectra of Pt and PtO_2 indicates that platinum in the SnO_2 films is present as PtO_2 in the composition range of 0.6—2.0 at.%. An increase in the platinum concentration to 6.3 at.% gives rise to reduced Pt clusters.

Depending on the composition of the gas phase, the intensity of the Pt L_{III} white line varies in parallel with the change in the conductivity of the samples.[36] The spectra of SnO_2(Pt) (2.0 at.% of Pt) recorded at 350 °C at different compositions of the gas phase are shown in Fig. 16. After exposure to a CO(0.09%)—N_2 gas mixture, the intensity of the white line decreases, which is indicative of reduction of PtO_2 to Pt. Analogous spectra were recorded for the SnO_2(Pt) film containing 0.6 at.% of Pt.

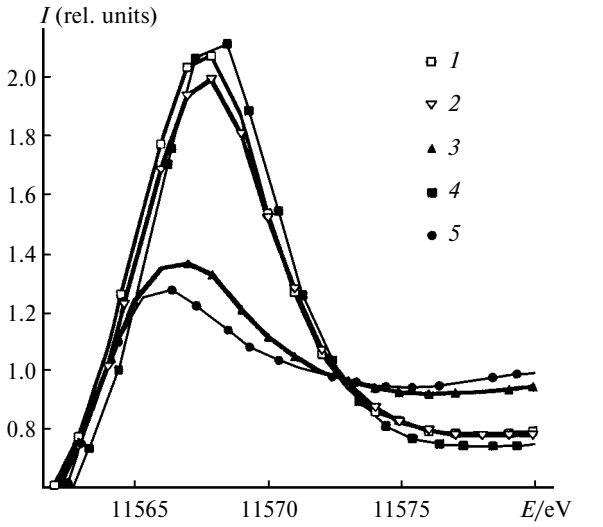

Fig. 15. XANES curves for SnO_2(Pt) films measured in air at 350 °C containing 0.6 (*1*), 2.0 (*2*), and 6.3 at.% of Pt (*3*), PtO_2 (*4*), and metallic Pt (*5*).[36]

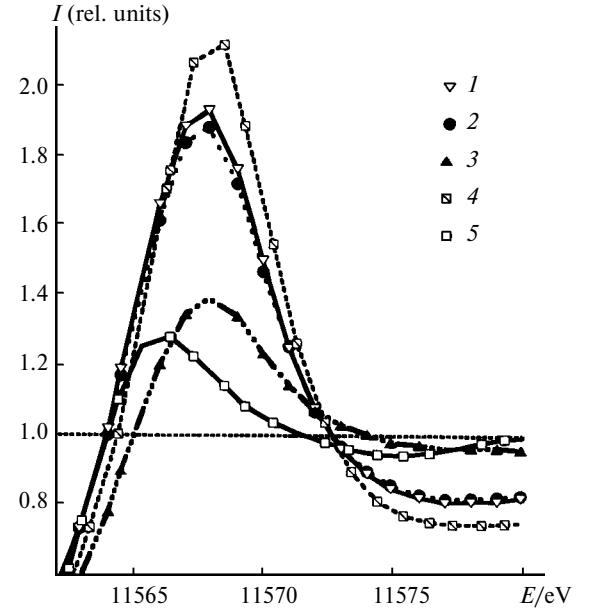

Fig. 16. XANES curves for SnO_2(Pt) film ([Pt] = 2.0 at.%) measured at 350 °C for different compositions of the gas phase: air (*1*), CO (0.03%) in air (*2*), CO (0.09%) in nitrogen (*3*), PtO_2 (*4*), and metallic Pt (*5*).[36]

Therefore, in SnO_2 films containing 6.3 at.% of platinum, the latter occurs in the reduced state regardless of the composition of the gas mixture used. In the films containing 0.6 or 2.0 at.% of Pt, the oxidation state of platinum changes depending on the composition of the gas phase. The size distribution of Pt aggregates depending on Pt concentration in SnO_2 films was studied by the TEM method.[44] It was found that the size of the clusters

increases with increasing Pt concentration. The weighted average sizes were 1.81, 1.84, and 2.33 nm for samples containing 0.6, 2.0, and 6.3 at.% of Pt, respectively. Presumably, Pt clusters on the surface of nanocrystalline SnO_2 catalyze oxygen exchange with the gas phase, the catalysis being most efficient when the particle sizes allow Pt to undergo complete reversible oxidation and reduction.

Raman spectroscopic study of *in situ* SnO_2(Cu) interaction with H_2S. Investigation of the mechanism of H_2S interaction with copper-doped SnO_2 is of particular interest because SnO_2(Cu) and SnO_2(Ni) films were found to possess exceptionally high sensitivity (10^3—10^4) toward H_2S (0.01%) at 100 °C (see Table 1, Refs. 18, 19, and 45—47), which suggests a substantial rearrangement of the nanocrystalline oxide surface and the possible occurrence of reversible chemical reactions involving copper.

A series of studies[9,48,49] were carried out with the use of a special measuring cell equipped with a quartz window, which enables one to record vibrational spectra simultaneously with conductivity measurements under the conditions of the controlled temperature and composition of the gas phase. All measurements were performed at 100 °C. An Ar laser (λ = 514.5 nm) was used as a radiation source. The beam was focused using a microscope objective (×50). The area of the region analyzed was ≤1 μm. The Raman spectra were recorded on a multichannel XY (Dilor) spectrometer.

The Raman spectra of nanocrystalline (spectra *1*—*4*) and microcrystalline (spectrum *5*) SnO_2 are shown in Fig. 17.[9,48] Samples of nanocrystalline SnO_2 were synthesized according to two procedures, *viz.*, by precipitation of an α-stannic acid gel as described above (hereinafter, SX samples) and by the cryosol method[27] (hereinafter, SK samples). Tin dioxide SK is characterized by a much larger specific surface and a higher concentration of the chemisorbed oxygen compared to SX samples. All samples were doped with copper by impregnation (see above). The characteristics of the samples are summarized in Table 9.[48] The spectrum of microcrystalline SnO_2 has three of four Raman-active lines in the spectra of single-crystalline SnO_2 corresponding to the rutile structure, *viz.*, E_g (476 cm^{-1}), A_{1g} (638 cm^{-1}), and B_{2g} (782 cm^{-1}). The spectrum of nanocrystalline SnO_2 has an additional line

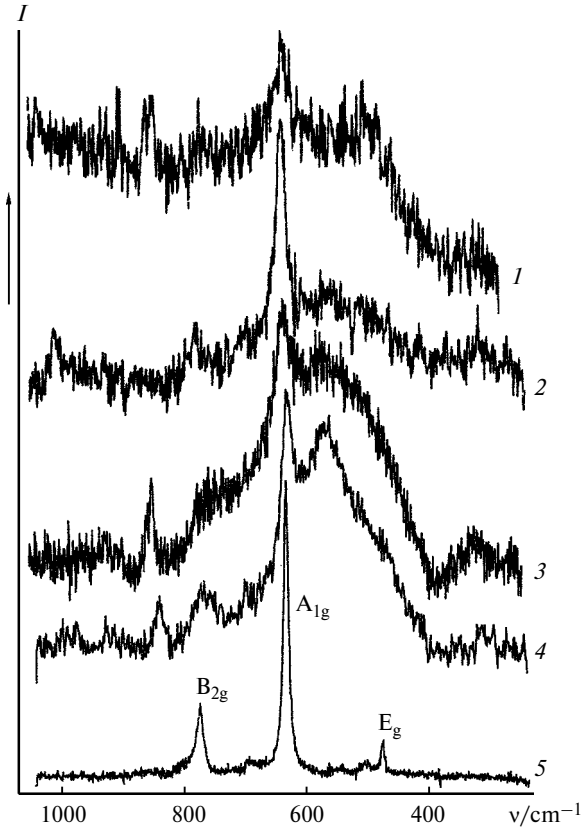

Fig. 17. Raman spectra of SnO_2: SX (*1*), SXCu5 (*2*), SK (*3*), SKCu5 (*4*), and microcrystalline SnO_2 (*5*).[9,48]

at 572 cm^{-1} belonging to vibrations of atoms on the SnO_2 grain surface. The complete assignment of the lines in the Ramam spectra of nanocrystalline SnO_2 was carried out in the earlier study.[9]

The effect of copper on the Raman spectra of nanocrystalline SnO_2 was studied for the SK samples containing 0, 1, 5, and 10 wt.% of Cu.[48] The observed shift of the maximum of the A_{1g} line (see Table 9) from 634 to 629 cm^{-1} (±1 cm^{-1}) is presumably associated with the contribution of CuO, which gives a signal in the region of 628—636 cm^{-1}.[50,51] A half-width of the A_{1g} line ($HW(A_{1g})$) increases, whereas the intensity of the surface mode, which is represented as the ratio between the in-

Table 9. Properties of pure and copper-doped SnO_2 samples[48]

Sample	[Cu] (wt.%)	$d(SnO_2)$ /nm	S_{sp} /$m^2\ g^{-1}$	$\nu_{A_{1g}}$ / cm^{-1}	$HW(A_{1g})$ / cm^{-1}	I_s/I_b	Interaction with H_2S			R/Ω (100 °C)	
							SO_4^{2-}	SnS_x	Cu_2S	Air	H_2S
SX	—	20	15	631			—	+	—	$4\cdot10^2$	$2\cdot10^2$
SXCu5	5			624			—	+	—	$2\cdot10^5$	$2\cdot10^3$
SK	—	4	170	634	10.5	8.5	+	+	—	$>10^8$	$5\cdot10^5$
SKCu1	1			634	10.6	11.5	—	—	—	—	—
SKCu5	5			633	13	2.5	+	+	+	$>10^8$	$4\cdot10^5$
SKCu10	10			629	14.5	2.5	—	—	—	—	—

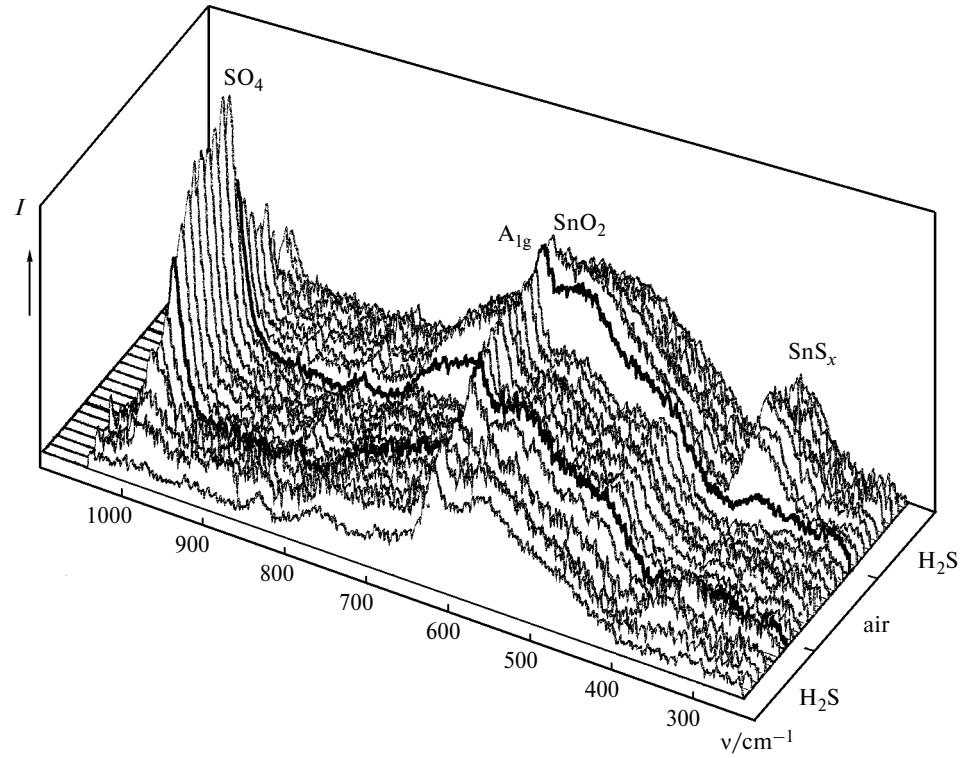

Fig. 18. Evolution of the Raman spectra of undoped tin dioxide SK as a function of a successive change in the composition of the gas phase at 100 °C.[49]

tensities of the surface mode (572 cm^{-1}) and the A_{1g} bulk mode (I_s/I_b), decreases with increasing copper concentration. The position of the A_{1g} maximum remains unchanged up to the copper concentration of 5 wt.%, whereas both the A_{1g} line width and the intensity of the surface mode change substantially as the copper concentration is increased from 1 to 5 wt.%. This may be indicative of the formation of copper oxide segregations on the SnO_2 grain surface.

Changes in the Raman spectra of undoped SnO_2 (SK) depending on the composition of the gas phase at 100 °C are shown in Fig. 18.[49] Unlike the spectra of the SX samples, the spectrum recorded after exposition to an H_2S atmosphere has a peak at 992 cm^{-1}. In addition, a weaker broad line appears at 350 cm^{-1}. This low-frequency line disappears in air, whereas the line at 992 cm^{-1} continues to increase up to saturation. At the same time, it should be noted that the intensity of the surface vibrational mode decreases. Subsequent exposition to an H_2S atmosphere leads to an instantaneous decrease in the intensity of the high-frequency mode simultaneously with an increase in the intensity of the broad line at 350 cm^{-1}, whereas the intensity of the surface mode reverts to its initial value.

Evolution of the Raman spectra of the SKCu5 sample as a function of the composition of the gas phase is presented in Fig. 19.[49] In addition to the spectral changes observed for undoped SnO_2, the introduction of copper leads to an increase in yet another line at 450 cm^{-1} in an H_2S atmosphere. The intensity of the latter mode decreases in air.

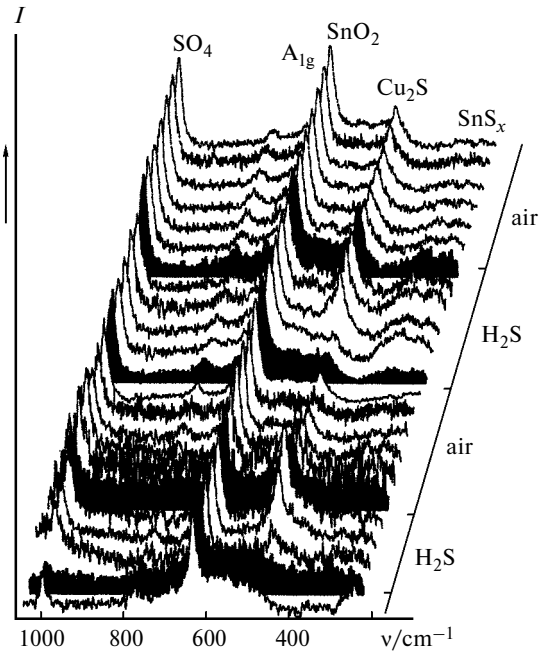

Fig. 19. Evolution of the Raman spectra of SKCu5 as a function of a successive change in the composition of the gas phase at 100 °C.[49]

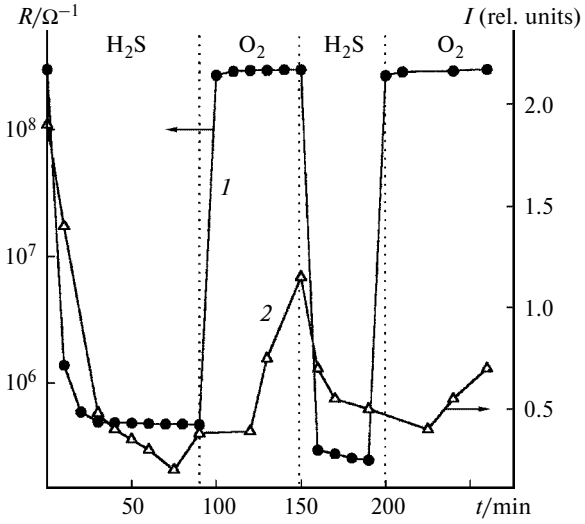

Fig. 20. Changes in the electrical resistance (*1*) and intensity of the A_{1g} mode (*2*) in the Raman spectrum of SKCu5 depending on the composition of the gas phase at 100 °C.[49]

Exposure to a reducing H_2S atmosphere leads to an instantaneous substantial decrease in the electrical resistance of the SK samples (Fig. 20, see Table 9). The electrical resistance of these samples again sharply increases immediately after the admission of air to the system. Figure 20 also presents the change in the intensity of the A_{1g} bulk mode consistent with the change in the conductivity of the samples.[48,49]

The intense high-frequency line at 992 cm^{-1} is indicative of the presence of SO_4^{2-} ions.[52] The frequency of the A_{1g} vibrational mode of the tetrahedral SO_4^{2-} ion varies from 960 to 1020 cm^{-1} depending on the nature of the cation. In the spectrum of commercial $SnSO_4$, the A_{1g} mode is observed at 970 cm^{-1} and it is more narrow than that observed in the spectra of SnO_2 samples. In this connection, it can be assumed that the appearance of this high-frequency mode is associated with the formation of the surface SO_4^{2-} groups. This hypothesis is supported by a decrease in the intensity of the surface vibrational mode simultaneously with an increase in the intensity of the 992 cm^{-1} band. The appearance of a broad low-frequency band in an H_2S atmosphere can be assigned to the formation of SnS, whose most intense mode is recorded at 300 cm^{-1}. As in the case of tin sulfate, the shift and broadening of this line can be attributed to the formation of surface SnS species. The appearance of the line at 450 cm^{-1} is, presumably, associated with the presence of Cu_2S. The thermodynamic estimates[48,49] demonstrated that the formation of tin sulfate under the experimental conditions is highly probable. At the same time, the possibility of the formation of tin and copper(I) sulfides is in doubt.

The formation of sulfate groups on surfaces of the SK samples may be accounted for by a high concentration of chemisorbed oxygen:

$$H_2S + 5\,(O^{2-})_{surf} = (SO_4^{2-})_{surf} + H_2O + 8\,e. \quad (9)$$

By contrast, a low concentration of chemisorbed oxygen on the surface of SX samples results in another mechanism of SnO_2 interaction with H_2S:

$$H_2S + 3\,O_O^x = H_2O + SO_2\uparrow + 3\,V_O^{\cdot\cdot} + 6\,e. \quad (10)$$

In the case of copper-doped SK samples, a substantial change in the electrical resistance in the presence of H_2S traces can be attributed to the formation of copper(I) sulfide, which is a narrow bandgap semiconductor:

$$6\,CuO + 4\,H_2S = 3\,Cu_2S + SO_2 + H_2O. \quad (11)$$

This reaction eliminates the energy barrier at the p-CuO/n-SnO_2 grain boundaries, with the result that the conductivity of the system increases. In the absence of H_2S molecules, copper sulfide in a nanocrystalline system, which is kept in air at 100 °C, is instantaneously transformed into CuO and the electrophysical properties of the system revert to the original state.

Mössbauer spectroscopic studies of SnO_2(Pd) interaction with CO. The role of palladium in the interaction of nanocrystalline SnO_2 with the gas phase was studied by ^{119}Sn Mössbauer spectroscopy.[28] Studies were carried out in a quartz reactor connected with a thin-walled quartz cell for recording Mössbauer spectra and a system for measuring the conductivity. The $Ca^{119}SnO_3$ compound was used as the γ-radiation source. The Mössbauer spectra were recorded using SnO_2 and SnO_2(Pd) (1 at.% of Pd) powders, which were preliminarily kept at constant temperature and a constant composition of the gas phase, rapidly cooled by placing the reactor in ice water, and then transferred to a thin-walled Mössbauer cell connected with the reactor. In the course of this treatment, exposure of the samples to air was excluded. The spectra were recorded at 100 K. The temperature, duration of exposure to the gas mixture under study, and the rate of gas flow through the cell were varied.

The Mössbauer spectra of the SnO_2(Pd) powder after annealing in dry air (*a*) or a CO(1%)—N_2 gas mixture (*b*) at 380 °C for 60 min (rate of the gas flow through the cell was 4 L h^{-1}) are shown in Fig. 21.[28] The parameters of the spectrum presented in Fig. 21, *a* (isomer shift $\delta = 0.00\pm0.02$ mm s^{-1}, quadrupole splitting $\Delta = 1.2\pm0.02$ mm s^{-1}) correspond to Sn^{IV} in the structure of crystalline SnO_2, which was used as the reference sample. Therefore, the nanocrystalline state of SnO_2 has no substantial effect on the electron density on the ^{119}Sn nuclei. Other components were not revealed in the spectrum. This is the difference between our data and the results of

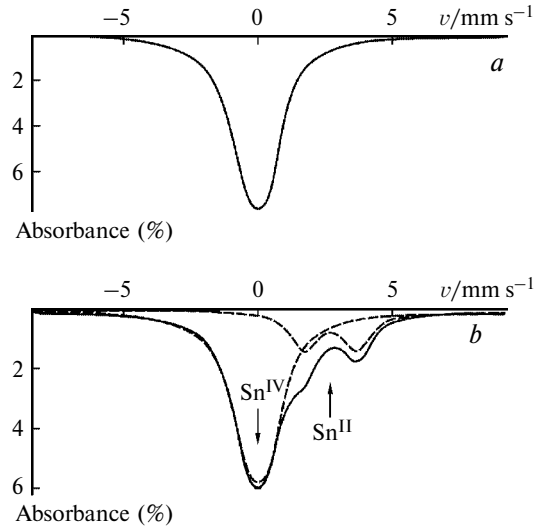

Fig. 21. Mössbauer spectrum of a SnO_2(Pd) powder after annealing in dry air (*a*) and a CO(1%)—N_2 gas mixture (*b*) at 380 °C.[28]

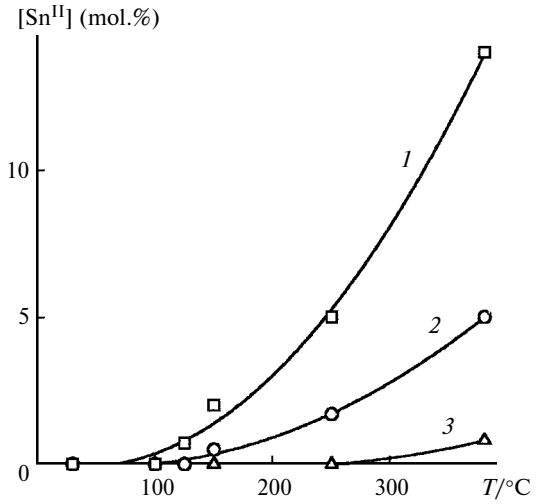

Fig. 22. Content of Sn^{II} in powders of nanocrystalline SnO_2(Pd) (*1*), nanocrystalline SnO_2 (*2*), and microcrystalline SnO_2 (*3*) depending on the annealing temperature in a CO(1%)—N_2 gas mixture.[28]

the Mössbauer spectroscopic study[53] in which an unknown compound containing the Pd—O—Sn bonds was found.

The spectra recorded after annealing of pure and doped SnO_2 in CO (see Fig. 21, *b*) show a doublet corresponding to Sn^{II}. It should be noted that the parameters of Sn^{II} (isomer shift $\delta = 2.74 \pm 0.04$ mm s^{-1}, quadrupole splitting $\Delta = 1.93 \pm 0.04$ mm s^{-1}) are indicative of the presence of a stereochemically active lone electron pair[54] and are close to the corresponding values for Sn^{II} occupying low-coordination positions on the surfaces of Cr_2O_3, V_2O_3, and α-Al_2O_3 crystallites.[55] After annealing in CO, tin metal was not detected. Analogous experiments were carried out at 25, 100, 125, 150, and 250 °C. The results of this study made it possible to estimate the Sn^{II} concentration in the samples (Fig. 22). For comparison, Fig. 22 demonstrates also the results of investigation of microcrystalline SnO_2 ($d > 500$ nm).[28] It was found that the reactivity of nanocrystalline SnO_2 is much higher than that of microcrystalline SnO_2.

The Sn^{II} content was estimated taking into account the known weight of a powder in the cell and the spectral contribution of Sn^{II} at 100 K after annealing in a CO-containing gas mixture. The spectral contribution of Sn^{II} was converted into the Sn^{II} concentration per square centimeter of the surface in the approximation of a thin adsorber layer taking the f' factor (Lamb—Mössbauer factor) for Sn^{II} as 0.75 (average value for Sn^{II} in the surface positions was calculated based on the effective Mössbauer temperatures θ_M published in the review[55]).

Annealing of SnO_2 and SnO_2(Pd) powders in a gas mixture containing 0.1% of CO in air at 373—653 K did not give rise to a signal of Sn^{II} in the Mössbauer spectra, which confirms the key role of oxygen in the mechanism of the sensor response of films.

The kinetics of the change in the conductivity of thick SnO_2 and SnO_2(Pd) films in CO and the change in the Sn^{II} concentration calculated from the Mössbauer spectra of the corresponding powders are compared in Fig. 23. The evolution of the spectrum of the SnO_2(Pd) sample in the course of interactions with CO and air is presented in Fig. 24. A rapid increase in the spectral contribution of Sn^{II} takes place immediately after the introduction of a CO(1%)—N_2 mixture into the system. By contrast, the introduction of air leads to rapid (<1 min) and complete oxidation of Sn^{II} to Sn^{IV}. Two main characteristic features should be noted: 1) the Sn^{II} concentration of 1 mol.% is sufficient for an increase in the conductivity of the SnO_2(Pd) film by a factor of more than 1000; 2) a further increase in the Sn^{II} concentration does not substantially change the conductivity of the films.

The changes in the conductivity of a SnO_2(Pd) film (1 at.% of Pd) and the Sn^{II} content with time, which were determined based on the data from Mössbauer spectroscopy of the corresponding powder measured with passing a flow of a CO(1%)—N_2 mixture through a cell, are compared in Fig. 25. The plot $G(t)$ shows two stages of an increase in the conductivity. The first stage (immediately after the introduction of CO into the system) does not lead to the appearance of the Sn^{II} signal in the Mössbauer spectra. An increase in the conductivity in the second stage is accompanied by an increase in the Sn^{II} concentration.

The model of the interaction of SnO_2(Pd) with CO includes reaction (5) along with the oxygen exchange between the gas phase, surface, and bulk of SnO_2 (see reactions (1)—(3)). The introduction of CO into the gas phase leads to an increase in the number of oxygen vacancies, an increase in the electron concentration in the sub-

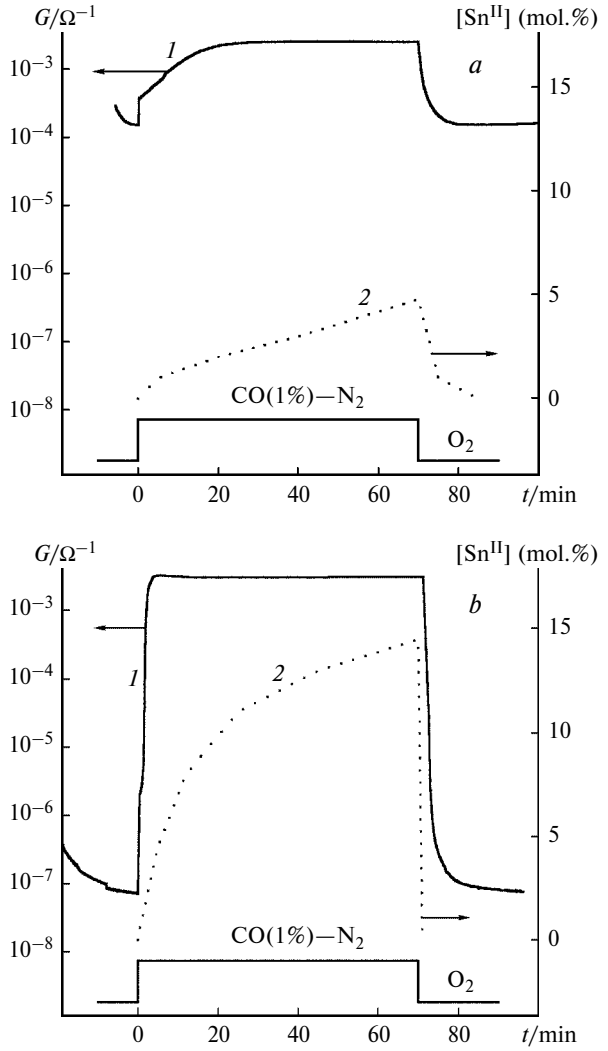

Fig. 23. Changes in the conductivity (*1*) of thick SnO_2 (*a*) and SnO_2(Pd) (*b*) films in a CO(1%)—N_2 gas mixture and the change in the Sn^{II} concentration (*2*) calculated from the Mössbauer spectra of the corresponding powders (gas flow was 4 L h^{-1}, T = 380 °C).[28]

surface layer, and a decrease in the height of the potential barriers at the SnO_2 grain boundaries. At T < 100 °C, diffusion of oxygen from the regular positions in the bulk of grains to their surface is the rate-determining step of the process.

The palladium clusters PdO_x can catalyze these surface reactions accompanied by an increase in the sensor signal:

$$PdO + CO = Pd + CO_2, \quad (12)$$

$$Pd + (O^{2-})_{surf} = PdO + 2\,e. \quad (13)$$

At high temperatures, the diffusion rate of oxygen is sufficiently high that the concentration of oxygen vacancies in the subsurface layer of SnO_2 remains constant. In this case, an increase in the conductivity by several orders of magnitude becomes possible only when the composition of SnO_2 grains reaches the homogeneity region boundary corresponding to the maximum oxygen deficiency. Apparently, this process is the initial step of reduction of the SnO_2 surface. Since SnO is a narrow bandgap semiconductor (E_g = 0.4 eV),[56] its formation on

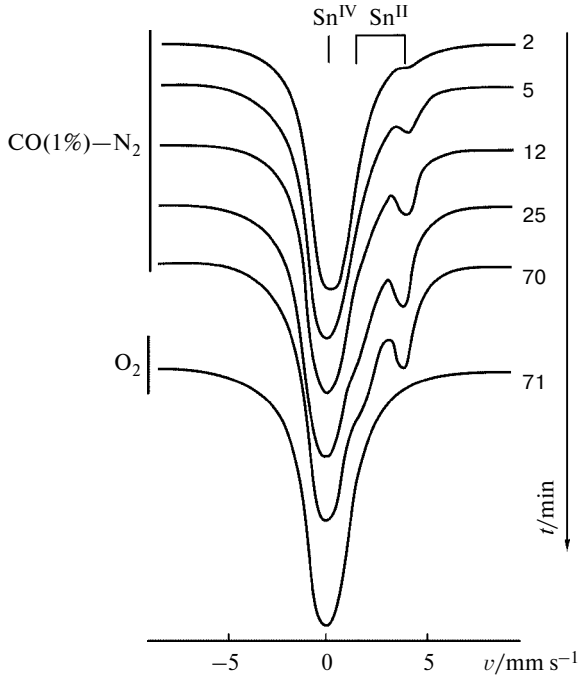

Fig. 24. Evolution of the Mössbauer spectrum of SnO_2(Pd) in the course of interaction with CO and air (gas flow was 4 L h^{-1}, T = 380 °C).[28]

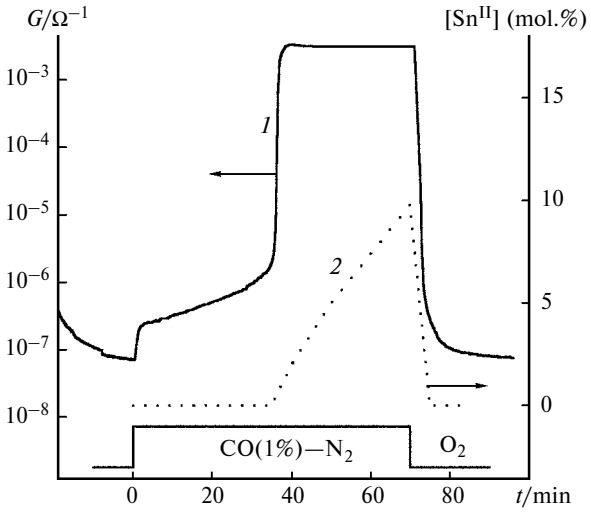

Fig. 25. Changes in the conductivity of a SnO_2(Pd) film (*1*) and the Sn^{II} content (*2*) according to the results of Mössbauer spectroscopy of the corresponding powder exposed to a CO(1%)—N_2 mixture (gas flow was 0.5 L h^{-1}, T = 380 °C).[28]

the SnO_2 surface can lead to a substantial increase in the conductivity.

Kinetics of interaction of SnO_2(M) with oxygen

The interactions of different gases with the SnO_2 surface involve either surface or lattice oxygen. The kinetics of the reaction with oxygen characterizes to a large extent the reactivity of nanocrystalline SnO_2. The influence of doping elements (M = Pd, Ru, Rh, Cu, or Ni) on the rate of reactions of nanocrystalline SnO_2 films with oxygen was studied *in situ* by conductivity measurements.[57] All the films were prepared by aerosol pyrolysis at 520 °C. The concentrations of dopant metals were in the range of 0.6—0.7 at.%. The kinetics of the change in the conductivity of the films was analyzed within the framework of the reaction-diffusion model.[58] It was assumed that the change in the conductivity of SnO_2 can be described by a model involving two successive steps, *viz.*, the linear diffusion of oxygen through pores of a nanocrystalline material and the interaction of oxygen with the SnO_2 grain surface.

If the linear diffusion of oxygen in the direction perpendicular to the film surface is the rate-determining step of the process, the time dependence of the conductivity can be approximated by the equation

$$G' = \frac{8}{\pi^2}\exp\left(-\frac{\pi^2 Dt}{4x_0^2}\right) = \frac{8}{\pi^2}\exp(-k_{dif}t), \qquad (14)$$

where $G' = (G_t - G_\infty)/(G_0 - G_\infty)$ is the normalized conductivity, G_t is its current value, G_0 is the maximum conductivity under a nitrogen atmosphere, G_∞ is the minimum conductivity under an oxygen atmosphere, and D is the diffusion coefficient of oxygen.[57,58]

If the surface reaction of a material with oxygen is the rate-determining step of the process under consideration, the following equation can be written on the assumption that the reaction follows the first-order kinetics:

$$G' = \exp(-k_r t). \qquad (15)$$

As can be seen from Eqs. (14) and (15), G' depends exponentially on the time in both cases. However, within the framework of the diffusion model (see Eq. (14)), the constant k_{dif} depends on the thickness of the film x_0, whereas there is no such a dependence for k_r within the framework of the reaction model (see Eq. (15)). Therefore, both cases can be represented as

$$G' = \exp(-kt), \qquad (16)$$

where k is the effective rate constant corresponding to the change in the conductivity of a material. The constant k can be estimated from the experimental time dependences of G'.

The rate-determining step was chosen based on the analysis of the dependence of k on the film thickness. It was found[57] that changes in the geometric parameters of films have no influence on the effective rate constant. Therefore, it can be assumed that the character of the change in the conductivity of nanocrystalline SnO_2 in an oxygen atmosphere is determined by rapid diffusion of oxygen in pores of a nanocrystalline film followed by slow chemisorption of oxygen on the SnO_2 grain surface.

The presence of dopant metals has a substantial effect on the constant k. The experimental time dependences of G' determined in oxygen after preannealing in nitrogen are shown in Fig. 26.[57] The maximum rate of the change in the conductivity was found for SnO_2(Ru) films. The constant k increases in the series $SnO_2 \approx SnO_2(Cu) < SnO_2(Ni) < SnO_2(Pd) < SnO_2(Rh) < SnO_2(Ru)$ (Fig. 27). Therefore, such metals as Ni, Pd, Rh, and Ru increase the rate of oxygen chemisorption on the SnO_2 surface. This fact may be associated with the spillover effect due to which clusters of platinum metals serve as concentrating agents for the subsequent migration of oxygen to the SnO_2 surface. High reactivities of platinum metals in the above-mentioned process have been observed earlier[59,60] in experiments on the $^{16}O/^{18}O$ oxygen isotope exchange in oxides SiO_2, Al_2O_3, ZrO_2, and TiO_2. The rate of the oxygen isotope exchange is most substantially affected by Ru and Rh. Studies by ESR spectroscopy demonstrated[61] that the concentration of the O_2^- paramagnetic centers on the SnO_2 surface increases in the presence of Ru and Pt. It is also known[62,63] that Ru, Rh, and Pd catalyze decomposition of NO_2 according to reaction (7) accompanied by the formation of O^{2-} on the

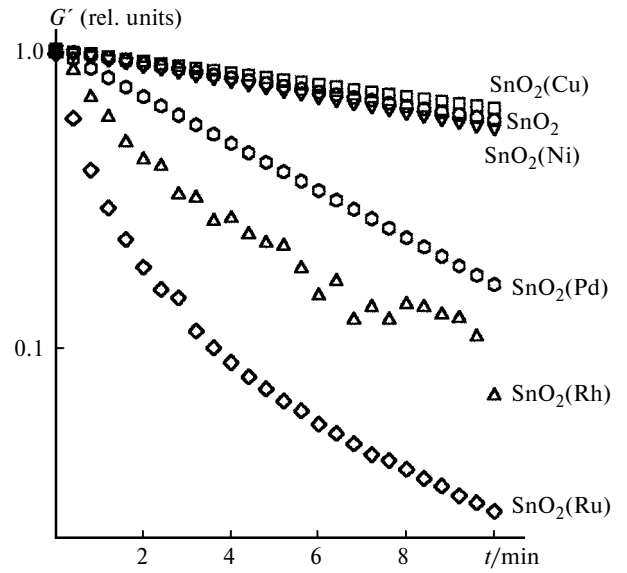

Fig. 26. Experimental time dependences of G' measured under oxygen after preannealing in nitrogen in the presence of different dopant metals in SnO_2(M) films.[57]

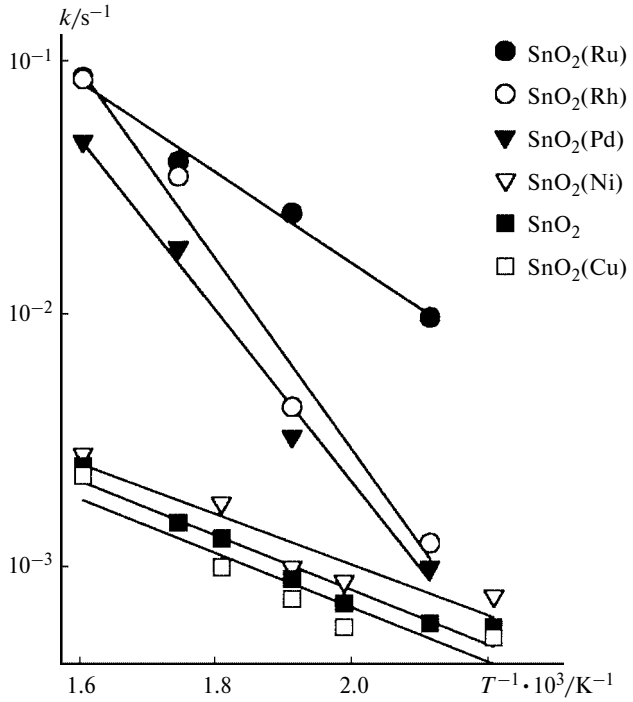

Fig. 27. Temperature dependences of the effective rate constant of the change in the conductivity of SnO_2 and SnO_2(M) films.[57]

surface of an oxide matrix, the kinetics of this process being dependent on the nature of the platinum metal. Therefore, the fact that SnO_2(Ru) films possess the highest sensor sensitivity toward NO_2 of all the materials studied by us (see Table 1) can be attributed to the maximum rate of electron exchange between SnO_2 and adsorbed species.

Electrophysical properties of doped SnO_2 films

To analyze the effect of doping elements on the energy spectrum of charge carriers in nanocrystalline SnO_2, the conductivity of films synthesized by aerosol pyrolysis was studied in the low-temperature range 77 K < T < 300 K. To prevent condensation of a water vapor on the film surface, the measurements were carried out under dry helium. The current was recorded in the mode of a stabilized voltage U, which was varied from 1 to 25 V. In this voltage range, the current-voltage characteristics of films are linear. The absence of the Schottky barrier between the film and gold contacts, which were applied by thermal evaporation *in vacuo*, was precontrolled using a special procedure (transmission line model) described in detail earlier.[64] In all the films under study, the electrical resistance of the contact was at most 5% of the resistance of the film.[65,66] Hence, the measured current can be considered as being proportional to the conductivity of the films. All measurements were carried out using a standard configuration (distance between the current contacts was 5 mm, the width of the films was 4 mm, and the thickness of the SnO_2 layer was 1 μm).

Figure 28 shows typical plots of log$R$ *vs.* $1/T$ for SnO_2(Cu), SnO_2(Pd),[67] and SnO_2(Ni)[68] films containing different amounts of doping elements. For SnO_2 films doped with other impurities considered in the present study, the $R(T)$ plots have analogous shapes.

Analysis of the temperature dependences of the electrical resistance revealed the following two main tendencies taking place upon doping of SnO_2: 1) resistance of films increases as the concentration of dopant metal is increased, 2) plots of log$R$ *vs.* $1/T$ have a linear region indicative of the activation character of the conductivity. Figure 29 presents the activation energy of the conductivity E_a calculated according to the Arrhenius equation *vs.* the concentration of the dopant introduced.[65–69] For the SnO_2(Cu) films, the energy E_a reaches the maximum (130 meV) at [Cu] > 1.5 at.%. This value of E_a is virtually equal to the ionization energy of the oxygen vacancies in single-crystalline SnO_2. Therefore, it can be assumed that the compensation of the donor effect of the oxygen vacancies by the acceptor copper centers in the bulk of nanocrystallites at [Cu] > 1.5 at.% is the main factor responsible for the mechanism of conductivity in SnO_2(Cu). In this case, the transport of charge carriers is determined primarily by the bulk rather than surface characteristics of nanocrystallites. It should be emphasized that the introduction of copper is the only instance when the plot of the energy E_a *vs.* the concentration of a dopant has a pronounced plateau.

In the presence of another acceptor dopant, *viz.*, Ni, the energy E_a increases monotonically as the nickel concentration in the film increases. It should be noted that the experimental energies E_a are substantially higher than 130 meV. It can be assumed that in these cases, the conductivity is determined by modulation of the band relief, which depends substantially on the charge state of the grain surface and intergrain boundaries.

The difference in the behavior of the conductivity upon doping of nanocrystalline SnO_2 with various acceptor impurities can be associated with the difference in the solubility of these dopants in a crystalline matrix in combination with the characteristic features of the formation of impurity states on the nanocrystallite surface. On the whole, these effects are typical of systems in which the electrophysical properties are determined by a superposition of the bulk and surface states. In particular, ultradispersed materials with a developed surface belong to the above-mentioned systems.

The addition of an acceptor dopant leads to a decrease in the electron concentration in the bulk of SnO_2 grains, a low-energy shift of the chemical potential, and a decrease in intergrain barriers under the conditions of a constant

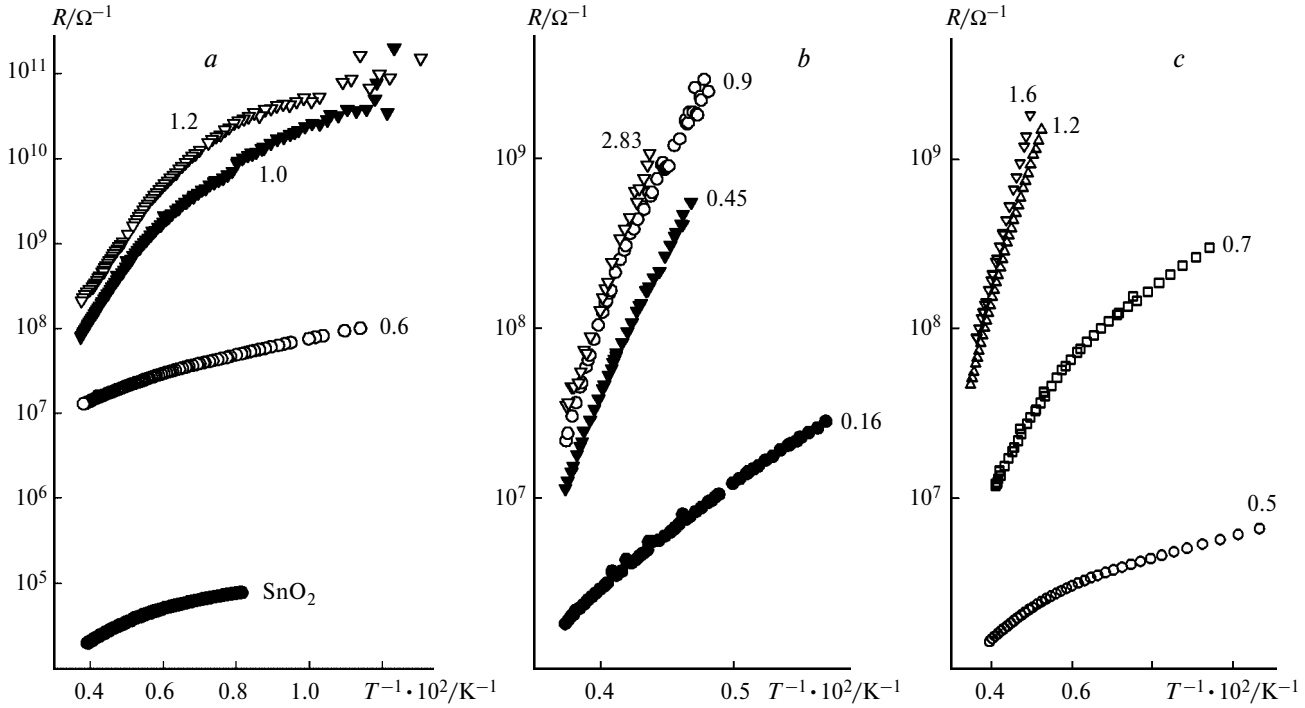

Fig. 28. Temperature dependences of the electrical resistance of SnO_2(Cu) (*a*),[67] SnO_2(Pd) (*b*),[67] and SnO_2(Ni) films (*c*).[68] The figures at the curves indicate the contents of doping elements (atomic percentage).

concentration of oxygen chemisorbed on the grain surface. In the case of the nondegenerate statistics of charge carriers, the activation energy corresponds to the ionization energy of the level characterized by a higher density of impurity states (in the case of SnO_2(Cu), the donor level of oxygen vacancies). However, the transfer of carriers within grains can be blocked if the conductivity of the grains is comparable to, or even lower than, the surface conductivity. This situation can take place both in the case of a high degree of compensation of the donor effect of oxygen vacancies by an acceptor impurity and upon the formation of a depletion layer, whose thickness is comparable to the grain size, at the crystallite boundaries. In the latter case, the transfer of charge carriers is determined by modulation of the band relief on the surface, and the energy E_a depends on activation of carriers to the mobility edge.

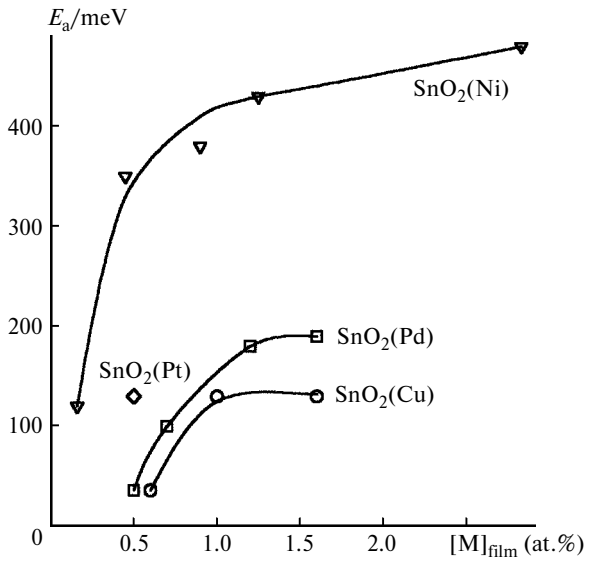

Fig. 29. Activation energy of conductivity (E_a) depending on the concentration of dopant metals $[M]_{film}$ in SnO_2(M) films.[65–69]

Since the ionic radius of Ni^{2+} is closer to that of Sn^{4+} as compared to Cu^{2+} (see Table 6), one would expect a higher solubility of nickel in the bulk of SnO_2 crystallites and, consequently, a more efficient compensation. It should be noted that E_a = 130 meV is observed in SnO_2(Ni) at an exceptionally low concentration of nickel in films: $[Ni]_{film}$ = 0.16 at.% (see Fig. 29). The peculiarities of the effect of nickel on the electrophysical properties were also observed in studies of the n-SnO_2(M)/p-Si heterostructures (M = Pd, Cu, or Ni).[68]

Analysis of the experimental data provided evidence that all known dopants are distributed among the bulk and surface of crystallites in different ratios. The Ni atoms are most likely to be located in the Sn positions in the bulk of crystallites. By contrast, the copper and palladium atoms form predominantly segregations on the SnO_2 grain surface. The grain boundaries make a contribution to an increase in the electrical resistance due to formation of barriers at the p-CuO/n-SnO_2 or p-PdO/n-SnO_2 boundaries.

* * *

The above-considered data demonstrate that the formal assignment of dopants in SnO_2 to either catalytic or electroactive dopants is somewhat simplified. Depending on the ionic radius and charge state, doping elements are differently distributed among the bulk and surface of nanocrystalline SnO_2 grains. In the SnO_2 matrix in air, all the dopants investigated in the present study occur in the oxidized state. The metallic state was detected only for Pt and Pd under a reducing atmosphere. The following general tendencies are observed upon the introduction of all the above-considered impurities:

1) decrease in the average size of crystalline SnO_2 grains, which can be caused by their segregation on the surface of SnO_2 crystallites resulting in the kinetic control over recrystallization;

2) increase in the electrical resistance of SnO_2 films; however, the changes in the conductivity can follow different mechanisms involving either the compensation of carriers or the formation of barriers at the grain boundaries characterized by different types of conductivity.

At the same time, dopants possess special properties. They can either be involved in specific chemical interactions with the gas analyzed (role of Cu and Ni in interactions with H_2S) or catalyze interactions of the SnO_2 matrix with the gas phase (Pt, Pd, Ru, or Rh).

This study was financially supported by the Russian Foundation for Basic Research (Project Nos. 01-03-32728, 02-03-06312, and 03-03-06609) and INTAS (Grant 2000-0066).

References

1. W. Gopel, *Sens. Actuators, A*, 1996, **56**, 83.
2. D. E. Williams, *Sens. Actuators, B*, 1999, **57**, 1.
3. N. Yamazoe and N. Miura, in *Chemical Sensor Technology*, Ed. S. Yamauchi, Kodansha, Tokyo, 1992, 19.
4. D. Kohl, *Sens. Actuators, B*, 1990, **1**, 158.
5. N. Yamazoe, *Sens. Actuators, B*, 1992, **6**, 9.
6. W. Fliegel, G. Behr, J. Werner, and G. Krabbs, *Sens. Actuators, B*, 1994, **18—19**, 474.
7. I. Matko, M. Gaidi, B. Chenevier, A. Charai, W. Saikaly, and M. Labeau, *J. Electrochem. Soc.*, 2002, **149**, H153.
8. G. K. Boreskov, *Kataliz. Voprosy teorii i praktiki. Izbrannye trudy* [*Catalysis. Theoretical and Practical Problems. Selected Works*], Nauka, Novosibirsk, 1987, 536 pp. (in Russian).
9. L. Abello, B. Bochu, A. Gaskov, S. Kudryavtseva, G. Lucazeau, and M. Rumyantseva, *J. Solid State Chem.*, 1998, **135**, 78.
10. T. Ressler, M. Hagelstein, U. Hatje, and W. Metz, *J. Phys. Chem., B*, 1997, **101**, 6680.
11. Z. M. Jarzebski and J. P. Marton, *J. Electrochem. Soc.*, 1976, **123**, 199C.
12. J. Mizusaki, H. Koinuma, J. I. Shimoyama, M. Kawasaki, and K. Fueki, *J. Solid State Chem.*, 1990, **8**, 443.
13. C. G. Fonstad and R. H. Rediker, *J. Appl. Phys.*, 1971, **42**, 2911.
14. J. F. McAleer, A. Maignan, P. T. Moseley, and D. E. Williams, *J. Chem. Soc., Faraday Trans. 1*, 1989, **85**, 783.
15. J. N. Zemel, *Thin Solid Films*, 1988, **163**, 189.
16. S. Lenaerts, J. Roggen, and G. Maes, *Spectrochim. Acta*, 1995, **51A**, 883.
17. O. V. Safonova, G. Delabouglise, B. Chenevier, A. M. Gaskov, and M. Labeau, *Mater. Sci. Eng., C*, 2002, **21**, 105.
18. M. N. Rumyantseva, M. Labeau, J. P. Senateur, G. Delabouglise, M. N. Boulova, and A. M. Gaskov, *Mater. Sci. Eng., B*, 1996, **41**, 228.
19. M. N. Rumyantseva, M. Labeau, G. Delabouglise, L. I. Ryabova, I. B. Kutsenok, and A. M. Gaskov, *J. Mater. Chem.*, 1997, **7**, 1785.
20. O. V. Safonova, M. N. Rumyantseva, R. I. Kozlov, M. Labeau, G. Delabouglise, L. I. Ryabova, and A. M. Gaskov, *Mater. Sci. Eng., B*, 2000, **77**, 159.
21. M. N. Rumyantseva, L. I. Ryabova, T. A. Kuznetsova, M. Labeau, G. Delabouglise, and A. M. Gas´kov, *Neorg. Mater.*, 1999, **35**, 68 [*Inorg. Mater.*, 1999, **35**, 54 (Engl. Transl.)].
22. M. N. Rumyantseva, A. M. Gaskov, L. I. Ryabova, J. P. Senateur, B. Chenevier, and M. Labeau, *Mater. Sci. Eng., B*, 1996, **41**, 333.
23. J. L. Pouchou and F. Pichoir, *Rech. Aerosp.*, 1984, **5**, 349.
24. B. Gautheron, M. Labeau, G. Delabouglise, and U. Schmatz, *Sens. Actuators, B*, 1993, **15—16**, 357.
25. A. V. Tadeev, G. Delabouglise, and M. Labeau, *Thin Solid Films*, 1999, **337**, 163.
26. H. Gleiter, *Acta Mater.*, 2000, **48**, 1.
27. S. M. Kudryavtseva, A. A. Vertegel, S. V. Kalinin, N. N. Oleynikov, L. I. Ryabova, L. L. Meshkov, S. N. Nesterenko, M. N. Rumyantseva, and A. M. Gaskov, *J. Mater. Chem.*, 1997, **7**, 2269.
28. O. Safonova, I. Bezverkhy, P. Fabritchny, M. Rumyantseva, and A. Gaskov, *J. Mater. Chem.*, 2002, **12**, 1174.
29. *Handbook of X-ray Photoelectron Spectroscopy*, Eds. C. D. Wagner, W. M. Riggs, L. E. Davis, and G. F. Moulder, Perkin Elmer Co, New York, 1979, 261.
30. M. S. Hegde and M. Ayyoob, *Surf. Sci.*, 1986, **173**, L635.
31. Y. Nagasawa, T. Choso, T. Karasuda, S. Shimomura, F. Ouyang, K. Tabata, and Y. Yamaguchi, *Surf. Sci.*, 1999, **433—435**, 226.
32. Q. Li, X. Yuan, G. Zeng, and S. Xi, *Mater. Chem. Phys.*, 1997, **47**, 239.
33. W. Epling, C. K. Mount, and G. B. Hoflund, *Appl. Surf. Sci.*, 1998, **134**, 187.
34. D. E. Ramaker, *J. Electron. Spectrosc. Relation Phenom.*, 1994, **66**, 269.
35. R. D. Shannon and C. T. Prewitt, *Acta Cryst.*, 1969, **B25**, 925.
36. M. Gaidi, J. L. Hazemann, I. Matko, B. Chenevier, M. Rumyantseva, A. Gaskov, and M. Labeau, *J. Electrochem. Soc.*, 2000, **147**, 3131.
37. M. Labeau, A. M. Gaskov, B. Gautheron, and J. P. Senateur, *Thin Solid Films*, 1994, **248**, 6.
38. G. B. Hoflund, *Chem. Mater.*, 1994, **6**, 562.
39. C. R. Henry, *Surf. Sci. Rep.*, 1998, **31**, 235.
40. *Fiziko-khimicheskie svoistva oksidov. Spravochnik* [*Physico-chemical Properties of Oxides. Handbook*], Ed. G. V.

Samsonov, Metallurgiya, Moscow, 1978, 472 pp. (in Russian).
41. J. O. Nell and H. St. S. O´Neill, *Geochim. Cosmochim. Acta*, 1996, **60**, 2487.
42. K. T. Jacob, T. Uda, T. H. Okabe, and Y. Waseda, *High Temp. Mater. Processes*, 2000, **19**, 11.
43. K. T. Jacob, S. Mishra, and Y. Waseda, *J. Am. Ceram. Soc.*, 2000, **83**, 1745.
44. I. Matko, M. Gaidi, J. L. Hazemann, B. Chenevier, and M. Labeau, *Sens. Actuators, B*, 1999, **59**, 210.
45. J. Tamaki, T. Maekawa, N. Miura, and N. Yamazoe, *Sens. Actuators, B*, 1992, **9**, 197.
46. S. Manorama, G. Salara Devi, and V. J. Rao, *Appl. Phys. Lett.*, 1994, **64**, 3163.
47. G. Salara Devi, S. Manorama, and V. J. Rao, *J. Electrochem. Soc.*, 1995, **142**, 2754.
48. T. Pagnier, M. Boulova, A. Galerie, A. Gaskov, and G. Lucazeau, *Sens. Actuators, B*, 2000, **71**,134.
49. T. Pagnier, M. Boulova, A. Galerie, A. Gaskov, and G. Lucazeau, *J. Solid State Chem.*, 1999, **143**, 86.
50. J. C. Irwin, J. Chrzanovski, T. Wei, D. J. Lockwood, and A. Wold, *Physica, C*, 1990, **166,** 456.
51. J. F. Xu, W. Li, Z. X. Shen, W. S. Li, S. H. Tang, X. R. Ye, D. Z. Jia, and X. Q. Xin, *J. Raman Spectrosc.*, 1999, **30,** 413.
52. S. D. Ross, in *The Infrared Spectra of Minerals*, Ed. V. C. Farmer, Mineralogical Society Monograph 4, The Mineralogical Society, London, 1974, p. 423.
53. F. Kh. Chibirova and E. E. Gutman, *Zh. Fiz. Khim.*, 1999, **73**, 292 [*Russ. J. Phys. Chem.*, 1999, **73** (Engl. Transl.)].
54. A. J. F. Boyle, B. S. P. Bunbury, and C. Edwards, *Proc. Phys. Soc. London*, 1962, **79**, 416.
55. M. I. Afanasov and P. B. Fabrichnyi, *Ross. Khim. Zh.*, 1996, **40**, 54 [*Mendeleev Chem. J.*, 1996, **40** (Engl. Transl.)].
56. B. P. Kryzhanovskii and A. Ya. Kuznetsov, *Zh. Fiz. Khim.*, 1961, **35**, 80 [*J. Phys. Chem. USSR*, 1961, **35** (Engl. Transl.)].
57. O. V. Safonova, M. N. Rumyantseva, M. Labeau, and A. M. Gaskov, *J. Mater. Chem.*, 1998, **8**, 1577.
58. J. W. Gardner, *Semicond. Sci. Technol.*, 1989, **4**, 345.
59. C. Descorme and D. Duprez, *Appl. Catal., A*, 2000, **202**, 231.
60. D. Martin and D. Duprez, *J. Phys. Chem.*, 1996, **100**, 9429.
61. C. Canevali, N. Chiondini, F. Marazzoni, and R. Scotti, *J. Mater. Chem.*, 2000, **10**, 773.
62. T. Jirsak, J. Dvorak, and J. A. Rodriguez, *Surf. Sci.*, 1999, **436**, L683.
63. K. D. Gibson, J. I. Colonell, and S. J. Sibener, *Surf. Sci.*, 1999, **443**, 125.
64. G. K. Reeves and H. B. Harrison, *IEEE Electron Dev. Lett.*, 1982, **5**, 111.
65. B. A. Akimov, A. M. Gas´kov, S. E. Podguzova, M. N. Rumyantseva, L. I. Ryabova, M. Labeau, and A. Tadeev, *Fiz. Tekhn. Polupr.*, 1999, **33**, 205 [*Semiconductors*, 1999, **33**, 175 (Engl. Transl.)].
66. B. A. Akimov, A. V. Albul, A. M. Gas´kov, V. Yu. Il´in, M. N. Rumyantseva, L. I. Ryabova, and M. Labeau, *Fiz. Tekhn. Polupr.*, 1997, **31**, 400 [*Semiconductors*, 1997, **31**, 335 (Engl. Transl.)].
67. O. V. Safonova, M. N. Rumyantseva, L. I. Ryabova, M. Labeau, G. Delabouglise, and A. M. Gaskov, *Mater. Sci. Eng., B*, 2001, **85**, 43.
68. R. B. Vasiliev, L. I. Ryabova, M. N. Rumyantseva, A. M. Gaskov, and B. A. Akimov, *Phys. Stat. Sol. (a)*, 2001, **188**, 1093.
69. B. A. Akimov, A. M. Gas´kov, M. Labeau, M. M. Osipova, M. N. Rumyantseva, and L. I. Ryabova, *Vestn. Mosk. Univ., Ser. Fiz. Astron.*, 1996, **37**, 60 [*Moscow Univ. Bull., Ser. Phys. Astron.*, 1996, **37** (Engl. Transl.)].

Received December 6, 2002;
in revised form February 20, 2003